Available online at www.sciencedirect.com

ScienceDirect

Geochimica et Cosmochimica Acta 199 (2017) 304–323

Geochimica et Cosmochimica Acta

www.elsevier.com/locate/gca

Redox reactions of selenium as catalyzed by magnetite: Lessons learned from using electrochemistry and spectroscopic methods

YoungJae Kim [a], Ke Yuan [a,1], Brian R. Ellis [b], Udo Becker [a,*]

[a] Department of Earth and Environmental Sciences, University of Michigan, 1100 North University Ave., Ann Arbor, MI 48109-1005, USA
[b] Department of Civil & Environmental Engineering, University of Michigan, 1351 Beal Ave., Ann Arbor, MI 48109-2125, USA

Received 30 March 2016; accepted in revised form 24 October 2016; available online 5 December 2016

Abstract

Although previous studies have demonstrated redox transformations of selenium (Se) in the presence of Fe-bearing minerals, the specific mechanism of magnetite-mediated Se electron transfer reactions are poorly understood. In this study, the redox chemistry of Se on magnetite is investigated over an environmentally relevant range of Eh and pH conditions (+0.85 to −1.0 V *vs.* Ag/AgCl; pH 4.0–9.5). Se redox peaks are found via cyclic voltammetry (CV) experiments at pH conditions of 4.0–8.0. A broad reduction peak centered at −0.5 V represents a multi-electron transfer process involving the transformation of selenite to Se(0) and Se(−II) and the comproportionation reaction between Se(−II) and Se(IV). Upon anodic scans, the oxidation peak centered at −0.25 V is observed and is attributed to the oxidation of Se(−II) to higher oxidation states. Deposited Se(0) may be oxidized at +0.2 V when pH is below 7.0. Over a pH range of 4.0–8.0, the pH dependence of peak potentials is less pronounced than predicted from equilibrium redox potentials. This is attributed to pH gradients in the microporous media of the cavity where the rate of proton consumption by the selenite reduction is faster relative to mass transfer from the solution.

In chronoamperometry measurements at potentials $\geqslant -0.6$ V, the current–time transients show good linearity between the current and time in a log–log scale. In contrast, deviation from the linear trend is observed at more negative potentials. Such a trend is indicative of Se(0) nucleation and growth on the magnetite surface, which can be theoretically explained by the progressive nucleation model. XPS analysis reveals the dominance of elemental selenium at potentials $\leqslant -0.5$ V, in good agreement with the peak assignment on the cyclic voltammograms and the nucleation kinetic results.

Keywords; Mineral redox catalysis; Magnetite; Selenium redox transformation; Se nucleation mechanism; Electrochemistry

1. INTRODUCTION

Magnetite (Fe_3O_4) is one of the most common ferrous oxide minerals in the Earth's crust (Ronov and Yaroshevsky, 1969). It occurs in diverse geological settings including igneous, metamorphic, and sedimentary units (Grant, 1985). Magnetite has unique ferrimagnetic properties and contains both ferric and ferrous iron in its structure. As a result, it plays a unique role in catalytically promoting redox reactions that may affect the short- and long-term geochemical cycles of iron and trace metals, such as Cr, As, or U, where the redox state sensitively affects the environmental behavior. In oxic aqueous environments, the ferrous iron (Fe^{2+}) present in magnetite may serve to reduce other redox-sensitive species in solution and form

* Corresponding author. Fax: +1 734 763 4690.
E-mail address: ubecker@umich.edu (U. Becker).
[1] Present address: Chemical Sciences and Engineering Division, Argonne National Laboratory, Argonne, IL 60439, USA.

http://dx.doi.org/10.1016/j.gca.2016.10.039
0016-7037/

ferric oxyhydroxides (White et al., 1994). The magnetite surface also provides specific adsorption sites for other solutes, which accounts for an interdependence of the iron geochemical cycle with that of many other elements (Stumm and Sulzberger, 1992). Gorski et al. (2012) recently reported that exchange of iron between the magnetite bulk structure and the aqueous phase is much more dynamic than previously believed and may be an important process in the sequestration and release of structurally incorporated trace metals.

While selenium (Se) is an important micronutrient for most life forms, it can be toxic at high concentrations. Its mobility, toxicity, and bioavailability are greatly influenced by its redox chemistry. Se is present in natural environments at +6, +4, 0, and −2 oxidation states in dissolved or solid form, and at the −1 oxidation state in some pyrite-like solids (*e.g.*, Williams and Byers, 1934). Se(VI) and Se(IV) (selenate and selenite, respectively) tend to be more soluble and toxic than Se(0) and Se(−II). Under highly reducing conditions in natural environments, Se(−II) is stable in solution as HSe^- and Se^{2-} or in solid phase metal selenides. H_2Se is stable only in highly acidic solutions.

The redox state of selenium can be influenced by microbial and abiotic processes in natural environments. The reduction of oxidized Se species to Se(0) is induced by microorganisms that metabolize organic matter in subsurface and aqueous environments (Lovley, 1993). Such microorganisms use oxidized selenium species as a terminal electron acceptor during the oxidation of organic matter. Analogous abiotic reduction of Se can be facilitated or catalyzed on mineral surfaces. The mechanisms for Se reduction by Fe-containing minerals are well described (Myneni et al., 1997; Bruggeman et al., 2005). Myneni et al. (1997) reported that reduction of Se(VI) to Se(0) occurs in the presence of green rust at rates comparable to those found in sediments. Green rust was demonstrated to mediate the reduction of Se(VI) via a heterogeneous process that includes adsorption or co-precipitation. The kinetics of Se reduction depends on the type of selenium species and mineral. For example, the reduction of oxidized Se to Se (0) by green rust or pyrite is slow whereas selenite is rapidly reduced by nanoparticles of magnetite and mackinawite (Scheinost and Charlet, 2008). These studies demonstrate that abiotic redox transformation mediated by Fe-bearing minerals can be an important process in the geochemical cycling of selenium in natural environments.

There have been attempts to adopt electrochemistry to investigate geochemical redox processes involving minerals. White et al. (1994) studied the dissolution kinetics of magnetite and observed the formation of an oxidized layer and the release of Fe(II) from the mineral structure into solution. A related study examined the reductive dissolution of magnetite in the presence of dissolved transition metals through use of potential dynamic voltammetry and found that the reduction of dichromate can suppress the reductive dissolution of magnetite (White and Peterson, 1996). The powder microelectrode (PME) method is commonly used to investigate electroactive materials and technological applications such as battery materials and fuel cells. So far, the application of the PME to study naturally occurring minerals has been limited but promising for the investigation of redox kinetics on surfaces (mainly oxides and sulfides). Renock et al. (2013) employed a standard three-electrode system equipped with PME to evaluate the thermodynamics and kinetics of U(VI) reduction by Fe oxides and sulfides. Yuan et al. (2015a,b) used a PME in concert with cyclic voltammetry experiments to discover that the disproportionation reaction mediated by U(V) is predicated upon the redox transformation of U(VI) on magnetite. Far fewer studies have addressed abiotic redox transformations of selenium mediated or catalyzed by magnetite (Scheinost and Charlet, 2008). The redox chemistry of Se has been examined for industrial purposes. For example, Se thin films are semiconducting and light sensitive such that they can be applied to devices such as solar cells, biological sensors, and light-emitting diodes (Lai et al., 2010; Saji and Lee, 2013). Although similar redox transformations may proceed upon interaction of Se with natural minerals, it is expected that specific mechanisms of Se redox behavior on minerals can be distinguished from those of industrially relevant materials (Saji and Lee, 2013). Moreover, little is known about Se electrochemistry over environmentally relevant pH value ranges because previous experiments have typically been performed in very acidic solutions (pH <2) pertinent to technical applications (Saji and Lee, 2013).

The goal of this investigation is therefore to use electrochemical techniques to identify and quantify reaction mechanisms and kinetics of the redox transformation of selenium mediated by magnetite at pH and Eh values commonly encountered in natural aqueous environments. The range of pH investigated was from 4.0 to 9.5 and the Eh range from +1.1 to −0.77 V (+0.85 to −1.0 V *vs.* Ag/AgCl). Cyclic voltammetry and chronoamperometry were performed using the magnetite electrode and collected data were analyzed to identify specific redox species responsible for electrical signals at given pH and Eh. X-ray photoelectron spectroscopy (XPS) was adopted to obtain direct evidence for Se redox reactions catalyzed by the magnetite electrode. In the discussion section, some of the results are revisited and discussed with quantitative evaluation including possible effects of solution chemistry on the Se redox transformation, mechanisms of Se nucleation derived by the magnetite electrode, and the catalytic role of magnetite in aqueous environments. By evaluating mechanisms and kinetics of heterogeneous redox reactions involving a mineral, this study intends to advance our understanding of the selenium redox transformation and catalytic effects of Fe-bearing minerals in subsurface environments.

2. MATERIALS AND METHODS

2.1. Magnetite electrodes

The powder microelectrode (PME) was prepared by conventional glass-blowing techniques with a Pt wire (100 μm in diameter) sealed in the center of the glass tube. In order to create the powder-filling cavity, the tip of the Pt wire was digested in *aqua regia* for 3 h at 80 °C. Further details about the PME preparation and usage can be found

in the literature (Cha et al., 1994; Cachet-Vivier et al., 2001; Renock et al., 2013; Yuan et al., 2015a,b). Although most experiments were performed using the PME, a bulk magnetite electrode (10–30 mm^2 in cross-sectional area) was prepared for specific experiments such as nucleation chronoamperometry and X-ray photoelectron spectroscopy (XPS). The preparation procedure for the bulk magnetite electrode was adopted from methods described by White et al. (1994) and Yuan et al. (2015b). Magnetite crystals (<5 mm in dimension) were polished with sand paper and thoroughly rinsed with Milli-Q water in order to remove any contaminants introduced through polishing. The samples were attached to copper wires using conducting silver paste and subsequently sealed, except for the exposed mineral surface, with an electronic-grade insulating epoxy.

Natural magnetite (Mineville, New York) was used for all experiments. X-ray diffraction (XRD) analysis confirmed that magnetite is the primary phase in the specimen. No treatment of the magnetite powder was performed to remove potential impurities prior to experiments. Although magnetite is a semiconductor, impurities can lead to a decrease in its conductivity. In order to ensure stable electrochemical signals for the PME, the natural magnetite was mixed with a graphite additive (10:1 magnetite/graphite ratio in mass) and ground using mortar and pestle. Such use of graphite to improve conductivity in PME experiments is well documented by Yuan et al. (2015b). The microcavity was packed with the magnetite powder by tapping the electrode cavity into the powder. The powder stayed in contact with the Pt wire during the experiment and was subsequently removed by sonication in 0.1 M $HClO_4$ solution after completion of each experiment.

2.2. Electrochemical experiments

In addition to the magnetite PME as the working electrode, a Pt wire served as the counter electrode and Ag|AgCl|1 M KCl (+0.235 V *vs*. standard hydrogen electrode, SHE, at 25 °C) was employed as a reference to compose a standard three-electrode cell. In the cyclic voltammetry (CV) measurements, voltammetric cycles were repeated until steady-state voltammetric responses were obtained. The potential range at which experiments can be performed without reducing or oxidizing the solvent differs between the electrode materials. The effective potential range for the Pt electrode in water is approximately −1.0 to +1.0 V *vs*. Ag/AgCl (Nurmi and Tratnyek, 2011). This range was used for all magnetite PME experiments. The scan rate for voltammetry experiments was set at 50 mV/s unless stated otherwise. Scanning at a higher rate was avoided because the irreversibility of Se redox reactions on magnetite increases with increasing scan rate, whereas scanning at lower rates leads to a decrease in the ratio of peak current to magnetite background current (see Section 3.1.2).

For electrochemical experiments, the Se(IV) solution was prepared by dissolving Na_2SeO_3 (Sigma Aldrich) in Milli-Q water with sodium perchlorate added as a background electrolyte to make solutions sufficiently conductive. The solutions were initially adjusted to the desired pH (4.0–9.5) by adding concentrated $HClO_4$ or NaOH. Prior to voltammetric scans, the solutions were purged with argon gas for 30 min to minimize the presence of dissolved oxygen and an argon headspace was maintained throughout each experiment. All electrochemical experiments were carried out at room temperature and atmospheric pressure.

2.3. XPS analysis

XPS spectra were collected using an Axis Ultra spectrometer (Kratos Analytical UK). A monochromic and focused Al $K\alpha$ radiation (1486.6 eV) was used for the excitation of samples. All measurements were performed in hybrid mode which employs both electrostatic and magnetic lenses. Survey and core scans were acquired at the constant pass energies of 160 and 20 eV, respectively. Measurements were performed under vacuum lower than 10^{-8} Torr. All spectra reported were calibrated using the position of the C 1s peak (286.4 eV) from adventitious carbon at the surface. Spectra analysis and calibration were performed using the CASA XPS software (version 2.3.16, www.casaxps.com).

3. RESULTS

3.1. Electrochemical characterization of selenium redox transformation

Magnetite behaves like a capacitor and typically exhibits a capacitance one or two orders of magnitude greater than electric double-layer capacitance (EDLC). Its pseudocapacitance arises mainly from Faradaic reactions involving surface or adsorbed species in aqueous electrolytes and is highly dependent on the type of aqueous electrolyte (Wu et al., 2003; Wang et al., 2006). Since the pseudocapacitance of magnetite results in large currents, electrochemical measurements were performed with the blank (*i.e.*, $NaClO_4$ only) and selenium solutions (Se(IV) + $NaClO_4$), separately, and the data were compared to distinguish electric signals of redox-active species from those of magnetite.

3.1.1. Cyclic voltammetry of magnetite microelectrode

The cyclic voltammetry of the magnetite PME was performed to examine current and electrochemical features of magnetite in blank solutions ($NaClO_4$ only) (Fig. 1). The cyclic voltammetry of magnetite was run at different pH values for 25 cycles (Fig. 1A). Since new magnetite samples were tested at each pH value, there was variation in current between the experiments. Nevertheless, the general patterns of the voltammograms are comparable between all magnetite PMEs. The complete voltammetric cycle shows a broad reduction shoulder centered near −0.3 V and two anodic peaks at −0.15 V and +0.4 V in agreement with previous reports on magnetite electrochemistry (Renock et al., 2013; Yuan et al., 2015b). For the anodic peak at +0.4 V, Yuan et al. (2015b) found that the peak potential and current increased when Fe(II) was added to the solution and proposed that the peak is attributed to the oxidation of ferrous to ferric iron. The cyclic voltammetry as a function of scan range is shown in Fig. 1B. The currents measured from

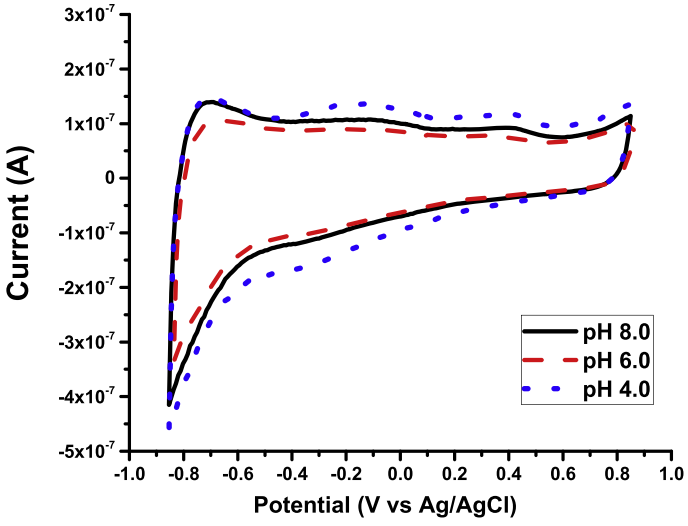

(A)

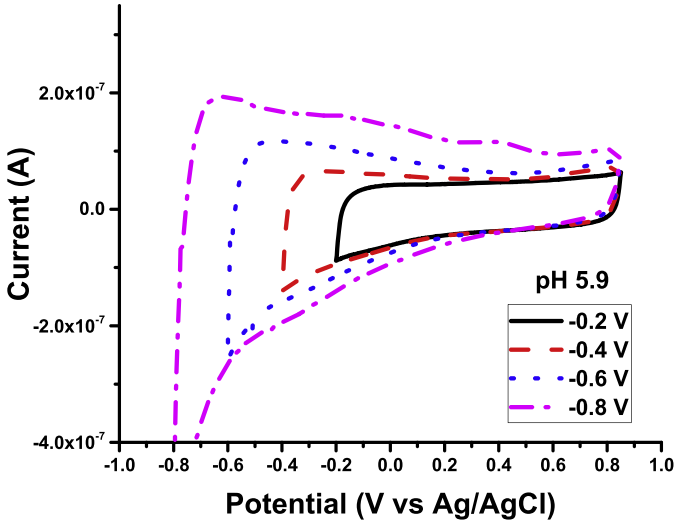

(B)

Fig. 1. Cyclic voltammograms of the magnetite PME in 0.05 M $NaClO_4$ (A) at the whole scan range with different pH values and (B) as a function of scan range at pH 5.9. Scan ranges are denoted by the negative switching potential values (−0.2 to −0.8 V) in the legend.

cathodic and anodic scans increase with increasing negative switching potential. The anodic peak at +0.4 V appears at switching potential lower than −0.7 V, indicating the occurrence of magnetite dissolution.

3.1.2. Cyclic voltammetry of selenium using a magnetite electrode

The cyclic voltammogram of Se(IV) as a function of pH and concentration is shown in Fig. 2. At pH 9.5, variations in Se(IV) concentration have little influence on the voltammogram, indicating no significant change in Se redox characteristics on magnetite (Fig. 2A). The voltammograms evidently evolve as the selenium concentration varies at pH values ⩽8.0. At pH 8.0, cathodic and anodic peaks are centered at about −0.5 and −0.25 V, and denoted by C1 and A1, respectively (Fig. 2B). Under acidic conditions (pH 4.0–6.0), there is only a small change in the peak position of C1 (−0.5 to −0.45 V). Upon anodic scans, peak A1 shows only a slight variation in potential (within a range of −0.3 to −0.2 V) and a new anodic peak, A2, develops near +0.2 V. At the pH range of 4.0–8.0, the anodic curves of different Se concentrations (1–25 mM) intersect with each other and the background curve (*i.e.*, [Se] = 0 mM) at about −0.6 V. The intersection can be interpreted as a potential where a transition between reductive and oxidative processes occurs as redox potential changes on the magnetite electrode. The total current measured on the magnetite electrode is a combination of the current rising from magnetite, which is the observed current in the background curve, and the current generated from Se redox

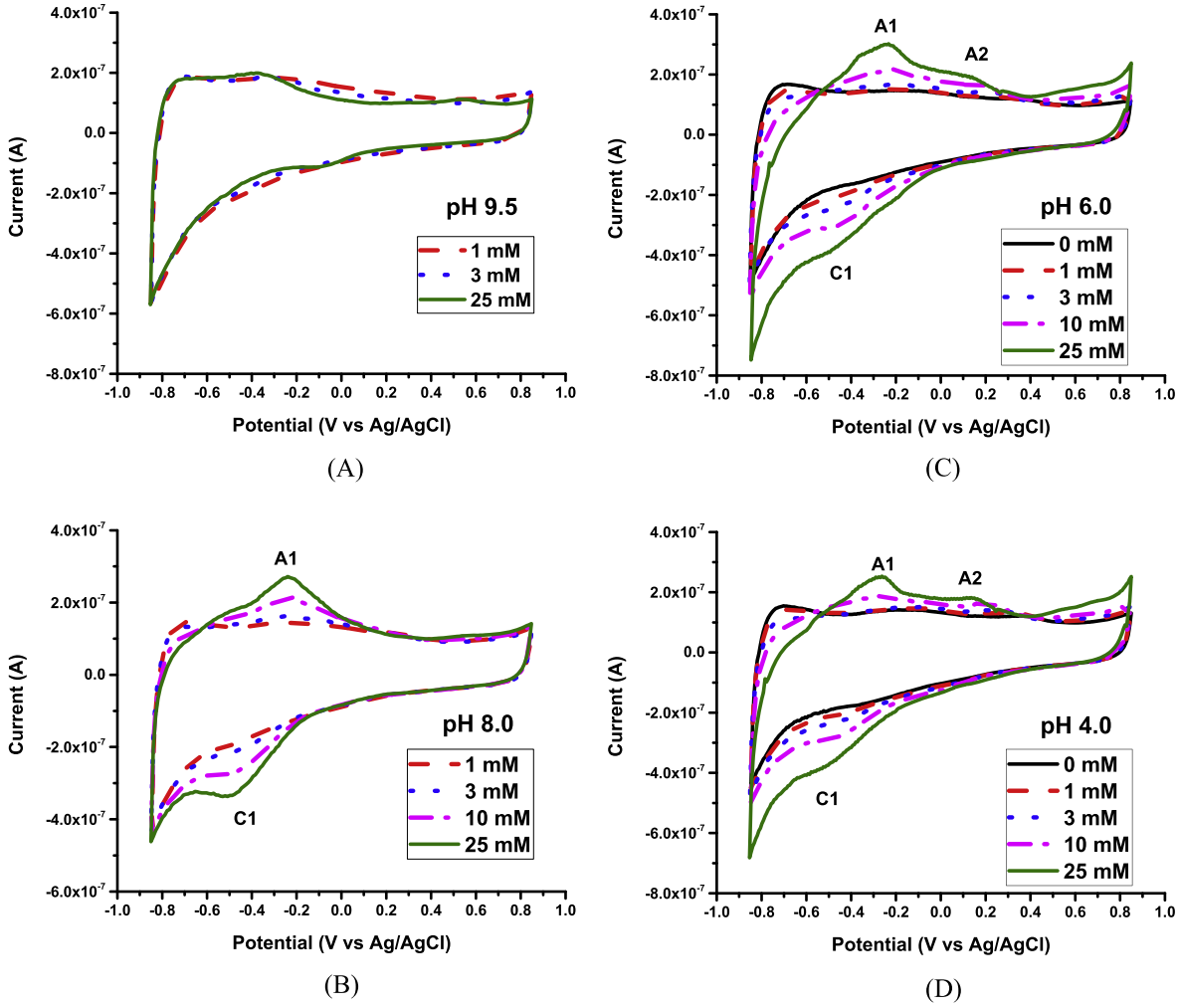

Fig. 2. Cyclic voltammograms for Se(IV) with the magnetite PME as a function of pH and the Se(IV) concentration (pH 4.0 to 9.5; [Se(IV)] = 1–25 mM). The solution contained 0.05 M $NaClO_4$ as a background electrolyte.

transitions. The total current is lower than the background current in the anodic potential region <-0.6 V, because electron-accepting processes of the electroactive species continue even upon anodic scanning. The total current is higher than the background current at potentials >-0.6 V where the electron-donating processes proceed. For all CV curves between pH 4.0–8.0, the peak currents of A1, A2, and C1 increase as the concentration of Se(IV) increases from 1 to 25 mM, confirming that the peaks are mainly due to redox processes involving Se during the positive and negative-going scans.

Cyclic voltammetry was performed at varying scan range in order to help identify individual redox peak pairs (Fig. 3). The aim of voltammetry using a narrow electrochemical potential range is to assign peaks describing corresponding redox couples observed upon cathodic and anodic scans. Coupling peaks may be obscured when scanning over a wide range of potentials if more than two peaks are produced as a result of cyclic voltammetry. This method of incrementally increasing scan ranges can be advantageous to resolve the CV curves where cathodic scans produce a broad peak region (*i.e.*, peak C1 in Fig. 2). In Fig. 3, the growth of anodic peaks A1 and A2 becomes pronounced as the switching potential increases. At pH 4.0–7.9, peak A1 starts to appear upon scans recorded at the switching potentials of -0.5 V and its peak current is further enhanced at more negative switching potentials. At pH 5.9 and 4.0, peak A2 begins to rise above background signals at a scan between -0.4 and $+0.85$ V. The switching potentials of -0.5 V for A1 and -0.4 V for A2, are both close to the peak potential of C1, thus implying that peak C1 is responsible for both peak A1 and A2. In this case, more than one reduction process takes place and the reduction products are oxidized at peaks A1 and A2. This explanation is plausible because the slow redox kinetics of selenium can cause multiple peaks to overlap and to be seen as a single broad peak (Renock et al., 2013). In summary, although peak C1 is centered at about -0.5 V, the peak is broad, ranging from -0.2 to -0.8 V (Fig. 2) and is likely the result of multistep charge transfer and slow Se redox chemistry.

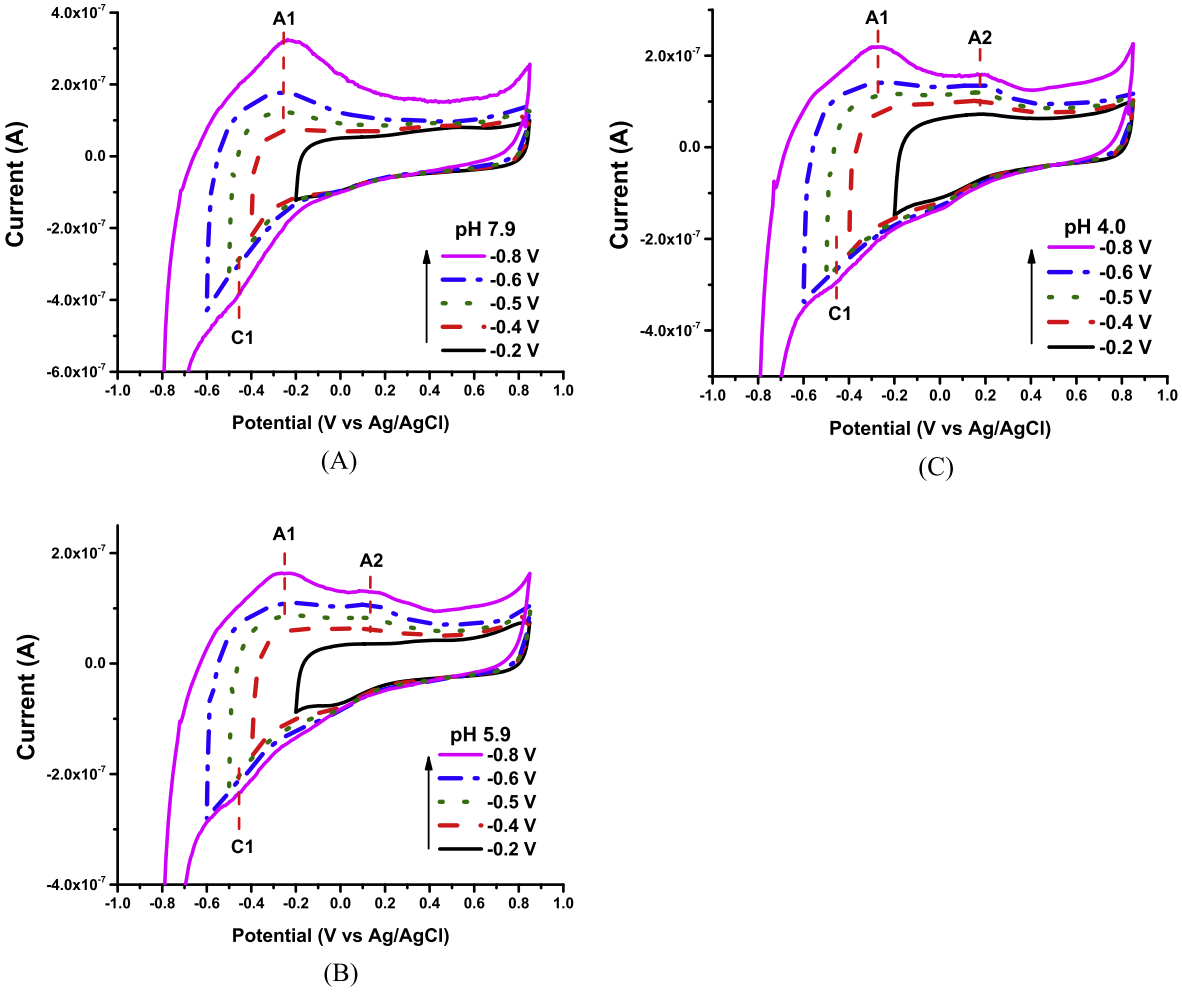

Fig. 3. Cyclic voltammograms for Se(IV) with the magnetite PME as a function of scan ranges. The scans were performed in a solution containing 10 mM Se(IV) and 0.05 M $NaClO_4$.

The kinetics of selenium transformation on the magnetite surface is further examined by performing cyclic voltammetry at varying scan rates (Fig. 4). The small size of the microcavity electrode (100 μm in diameter and a few tens of μm deep) in this study allows performing cyclic voltammetry over a large range of scan rates (25–250 mV/s). The CV curves remain stable at rates ⩽250 mV/s. The peak currents increase with increasing scan rate and the least-square fits show excellent linearity ($R^2 > 0.98$) between the current and the square root of the scan rate (Fig. 4C). Upon increasing the scan rate, the cathodic and anodic peaks are shifted by about 0.1 V to more negative and positive potentials, respectively (Fig. 4D). Irreversibility of Se redox processes on magnetite is indicated by the fact that the positions of cathodic and anodic peaks are highly dependent of the scan rate (Nurmi and Tratnyek, 2011). The role of slow kinetics in Se redox irreversibility is further substantiated by other features from the cyclic voltammetry results such as the broad peak widths and deviation of the peak potentials from the corresponding equilibrium reduction potentials (Fig. 2 and Section 3.1.3) (Bard and Faulkner, 1980).

3.1.3. Redox transformation of selenium on magnetite

Se(IV) in the bulk solution can be converted into Se(VI), Se(0), and Se(−II) during cyclic voltammetry scans. To investigate Se redox transformations on the magnetite surface, possible selenium redox reactions and their reduction potentials were considered (Table 1 and Fig. 5). The Se(IV) speciation (protonation stage) was calculated for pH 2–12 as shown in Fig. 6. Biselenite ($HSeO^{3-}$) and biselenide (HSe^-) are the dominant selenium species between pH 4.0–8.0 where electrochemical peaks indicating selenium redox transformation are found (Figs. 2 and 6). The oxyanion of Se(VI), selenate is a very weak base ($pK_{a2} = 1.7$) and is present mainly as a deprotonated species, SeO_4^{2-} at pH >2. Based on this speciation, half reactions of the dominant Se species as reactants or products were derived as a function of pH (Table 1). The half reactions of these redox couples indicate that the reduction of selenium species is thermodynamically favored under acidic conditions. The equilibrium reduction potential (E_{eq}) equation of each half reaction was calculated from the Nernst relation (Eq. (1)) to identify the redox processes responsible for the observed CV peaks (Table 1).

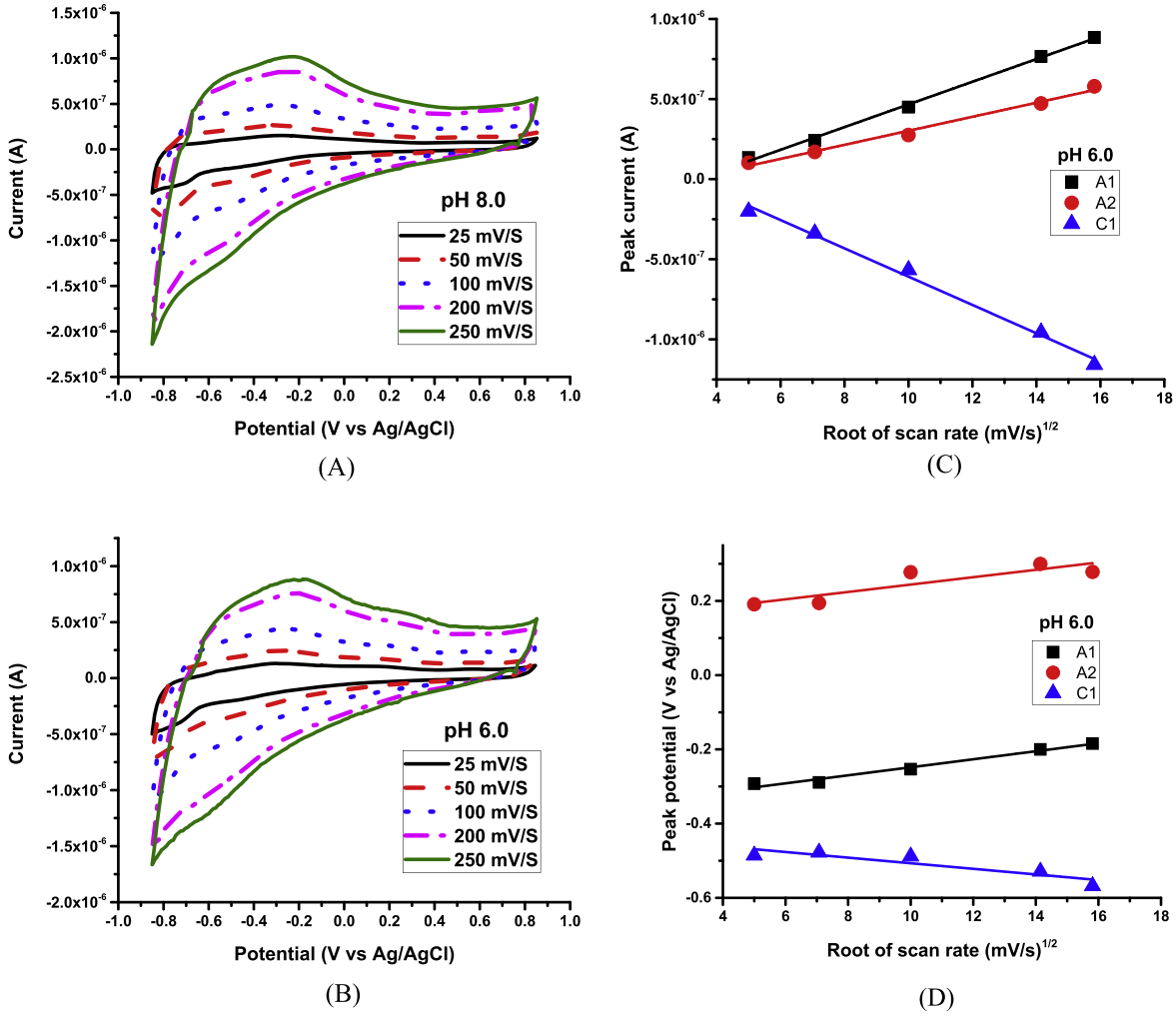

Fig. 4. Cyclic voltammograms as a function of scan rate (25 to 250 mV/s) (A) at pH 8.0 and (B) at pH 6.0. For pH 6.0, (C) peak currents and (D) potentials were plotted and the linear least-square fits were added to show their trends. The scans were performed in a solution containing 10 mM Se(IV) and 0.05 M $NaClO_4$.

Table 1
Reduction potential equations for possible redox reactions of selenite as a function of pH. Reactions I to IV are denoted in text by abbreviated forms indicating the oxidation state, Se(IV)/Se(0), Se(IV)/Se(−II), Se(0)/Se(−II) and Se(VI)/Se(IV), respectively.

	Standard reduction potential* (*vs.* Ag/AgCl)
(I) $HSeO_3^- + 5H^+ + 4e^- = Se(s) + 3H_2O$	$E^0 = 0.54$ V
$E = 0.54 - 0.074\ pH + 0.015\ \log[HSeO_3^-]$	
(II) $HSeO_3^- + 6H^+ + 6e^- = HSe^- + 3H_2O$	$E^0 = 0.11$
$E = 0.11 - 0.059\ pH + 0.010\ \log[HSeO_3^-]/[HSe^-]$	
(III) $Se(s) + H^+ + 2e^- = HSe^-$	$E^0 = -0.75$
$E = -0.75 - 0.030\ pH - 0.030\ \log\ [HSe^-]$	
(IV) $SeO_4^{2-} + 3H^+ + 2e^- = HSeO_3^- + H_2O$	$E^0 = 0.84$
$E = 0.84 - 0.089\ pH + 0.030\ \log\ [SeO_4^{2-}]/[HSeO_3^-]$	

* Adopted from Bouroushian (2010).

$$E_{eq} = E^0 + \frac{RT}{nF} ln \frac{a_O}{a_R} \quad (1)$$

where E_{eq} is the equilibrium reduction potential, E^0 the standard reduction potential, R the universal gas constant, T the temperature in Kelvin, n the stoichiometric number of electrons involved in an electrode reaction, F the Faraday constant, and a_O and a_R, the product of activities of all oxidants and reactants, respectively. Although the standard potential may serve as a similar indicator, the equilibrium

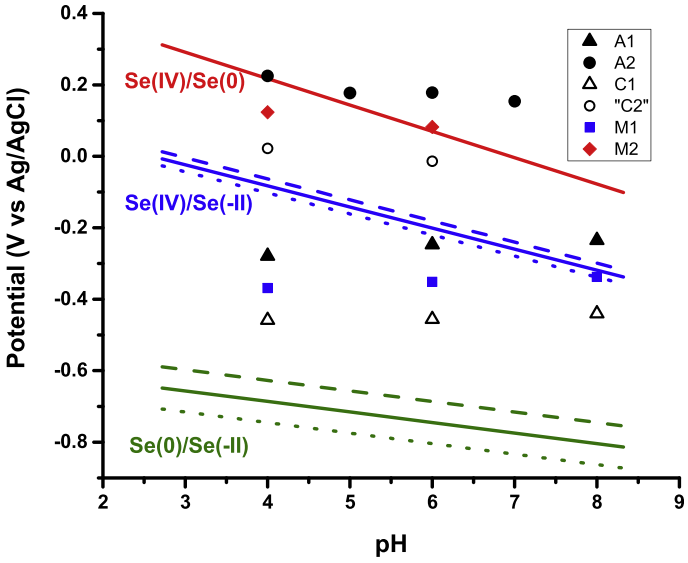

Fig. 5. pH dependence of observed CV peaks and theoretical equilibrium reduction potentials for selenium redox transformation. The peak potential data were collected from the cyclic voltammetry performed in solution containing 10 mM Se(IV) and 0.05 M $NaClO_4$. Lines are equilibrium reduction potentials of the redox couples, Se(IV)/Se(0) (red), Se(IV)/Se(−II) (blue) and Se(0)/Se(−II) (green) where $[HSeO_3^-]$ = 0.01 M and $[HSe^-] = 10^{-4}$–10^{-8} M (dashed, 10^{-4} M; solid, 10^{-6} M; dotted, 10^{-8} M). (For interpretation of the references to color in this figure legend, the reader is referred to the web version of this article.)

reduction potential is suitable in this study where the solution chemistry departs from the standard state (*i.e.*, the concentrations of solutes and proton ≪1 M). It is a reasonable assumption that the initial Se(IV) concentration (0.01 M) is approximately equal to $[HSeO_3^-]$ at a pH range of 4.0–8.0. In the bulk solution (50 mL in this study), other selenium species can only be produced from the Se(IV) redox reactions in the microcavity and therefore, their concentrations would be minute. In Fig. 5, the reduction potential lines are where $[HSeO_3^-]$ is 10^{-2} M and the concentrations of other selenium species are from 10^{-4} to 10^{-8} M. All four redox couples considered show a decrease in their equilibrium reduction potentials with increasing pH.

When comparing reduction potentials measured using CV curves with theoretical equilibrium reduction potentials, determination of the midpoint potentials, *i.e.*, the average of cathodic and anodic peak potentials ($E_{mid} = (E_{cath} + E_{anod})/2$) is typically used because the mid potential is approximately equal to the equilibrium reduction potential for reversible redox couples (Renock et al., 2013; Yuan et al., 2015b). This means that for both anodic peaks (A1 and A2), corresponding cathodic peaks have to be identified. Accurate measurements of reduction potentials using mid peak potentials are obscured by the fact that cathodic peaks, especially the ones corresponding to A2, cannot be clearly identified in all CV curves, partly because they are less sharp than the anodic ones. Nevertheless, for the sake of comparing theoretical reduction potentials with measured midpoint potentials, some data points "C2" (the quotation marks indicating the caveats described above), and the corresponding midpoint potentials are given in Fig. 5. The midpoint potentials of pairs A1/C1 and A2/"C2" are close to the theoretically-derived reduction potentials of the Se(IV)/Se(−II) and Se(IV)/Se(0) couples, respectively, but the association of the peaks with the selenium redox couples can be more complicated (Table 1). First, one needs to consider if either of the trends for Al and A2 peaks can be associated with the Se(VI)/Se(IV) couple. Alanyalioglu et al. (2004) reported that a pair of peaks corresponding to Se(VI)/Se(IV) redox pair was not observed when a scan range is made more negative than +0.3 V because of the formation of elemental Se from adsorbed selenite ions. Such a tendency of the Se(VI)/Se(IV) pair is contrasted with the trend for peak A1 and A2 in this study where an increase of peaks A1 and A2 with scanning at more negative potentials was observed (Fig. 3). Since the initial solution is prepared with sodium selenite, reduced species Se(0) or Se(−II) are likely to form under negative potentials and oxidation of Se(IV) to Se(VI) can be excluded as a peak assignment for these two anodic peaks.

Since the peak potential values of A2 are comparable to reduction potentials of the Se(IV)/Se(0) couple, it may be tentatively assigned to the oxidation of Se(0) to Se(IV) (Fig. 5). Lai et al. (2010) studied electrodeposition of Se(IV) onto the SnO_2 electrode using cyclic voltammetry in an acidic solution (pH ≈2). The oxidation peak at +0.25 V (*vs.* Ag/AgCl) was assigned to the oxidation of Se(0) to Se(IV). Although the electrode material and solution chemistry differed, the values reported by Lai et al. (2010) are comparable to the A2 peak potential of this study (+0.2 V at pH 4.0). Although peak C1 is centered at −0.5 V, the peak is very broad (from −0.2 to −0.8 V) and can reflect multistep charge transfer on the electrode (Section 3.1.2). The potential of −0.5 V is more negative than the equilibrium reduction potentials of the Se(IV)/Se(0) and Se(IV)/Se(−II) couples (Table 1 and Fig. 5). Despite no further thermodynamic evidence, the comparison with the equilibrium reduction potentials supports the peak

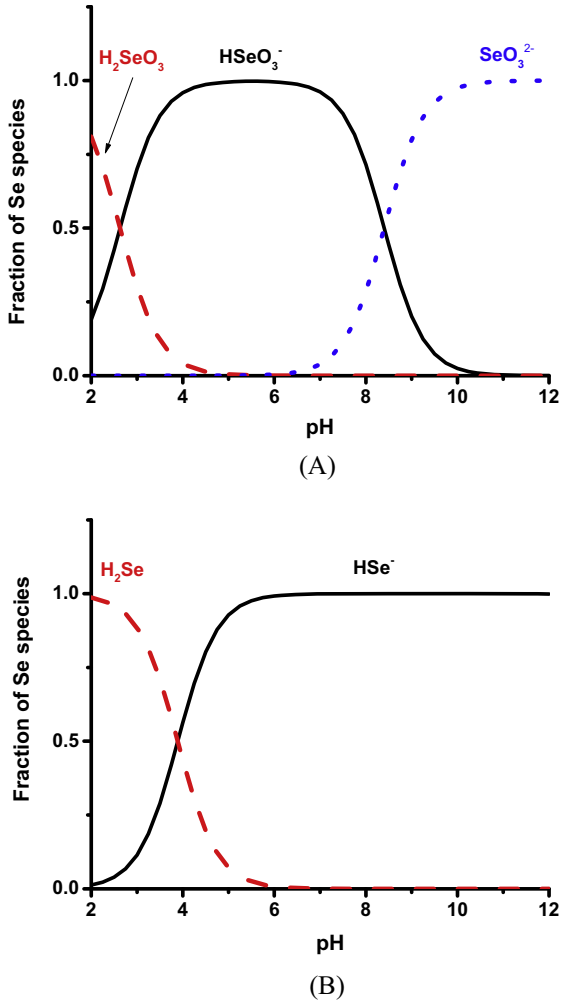

Fig. 6. Speciation of (A) Se(IV) and (B) Se(−II) as a function of pH ([Se] = 0.01 M). It is noted that biselenite ($HSeO_3^-$) and biselenide (HSe^-) are the most dominant species over a range of solution pH 4.0–8.0.

potential of C1 accounting for the formation of Se(0) and Se(−II) over the pH range of this study. An analogous interpretation was made in a previous study for selenite reduction on a gold electrode (Wei et al., 1994), which assigned a peak at −0.5 V to a combination of Se bulk deposition and Se(−II) formation. There is an overall consensus that Se(−II) species are produced from the reduction of Se(IV) (*e.g.*, Wei et al., 1994; Santos and Machado, 2004; Lai et al., 2010; Saji and Lee, 2013). Two different mechanisms have been proposed for the formation of Se(−II) (Lai et al., 2010; Saji and Lee, 2013). The first one is that Se(−II) is produced from further reduction of deposited Se(0). This can be described for our solution chemistry as a two-step process, equation I followed by equation III in Table 1. The second scheme is the formation of Se(−II) directly from Se(IV) as seen from equation II in Table 1. As the potential goes more negative than −0.5 V, the direct conversion from Se(IV) to Se(II) becomes more likely, but the production of Se(−II) from Se(0) may also proceed at very negative potentials (<−0.7 V). When Se(−II) is produced from either process, a subsequent comproportionation reaction can proceed in Se(IV)-containing solutions (Wei et al., 1994; Santos and Machado, 2004):

$$2HSe^- + HSeO_3^- + 3H^+ \leftrightarrow 3Se^0 + 3H_2O \text{ or}$$
$$2HSe^- + HSeO_3^- \leftrightarrow 3Se^0 + 3OH^- \quad (2)$$

The broad cathodic peak at C1 can explain different Se redox transformation processes: Se(IV) → Se(0) (→Se(−II)), Se(IV) → Se(−II), and Se(−II) → Se(0). Therefore, the observed cathode peak broadening may reflect that the selenium redox transformation on magnetite occurs through multiple processes.

The oxidation of Se(−II) and Se(0) may occur more and more as the anodic scan proceeds. The cyclic voltammetry as a function of scan range reveals that the peak current of A1 is associated with the species produced at C1 (Fig. 3). The equilibrium reduction potential data suggests that the peak potential of Al (−0.2 to −0.25 V) may account for the oxidation of Se(−II) to Se(IV) or to Se(0) (Fig. 5). In a similar manner, it is inferred that the oxidation of Se(0) may proceed at the potential corresponding to peak A2 as the scan goes more positive.

Although our peak assignment based on the thermodynamic data is consistent with previous studies and spectroscopic data (Section 3.2), the pH dependence of the CV peaks measured using a PME is less pronounced than that expected from the corresponding half reactions (Fig. 5). This may be caused by the pH in the microcavity continuously changing during potential scans whereas the bulk solution pH (that is used to calculate expected peak positions from half reactions) is almost invariable throughout the experiment. This pH gradient between the bulk solution and pores in the powder where redox transitions (and implicit pH changes) take place, leads to a peak broadening and potential shift of peaks relative to peak positions when the bulk solution pH is applied. Such considerations are revisited and discussed further in Section 4.1.

3.1.4. Chronoamperometry and nucleation kinetics

The kinetic aspects of selenium reduction processes on magnetite were examined using chronoamperometry over a negative potential range (0.0 to −1.0 V). Chronoamperometry measures current as a function of transient time when a potential is stepped between potentials on the working electrode. Two different solutions were prepared to differentiate the current from electroactive species and the capacitance current from electrolyte species acting on the magnetite surface: a selenium solution (10 mM Na_2SeO_3 + 0.1 M $NaClO_4$) and a blank solution (0.1 M $NaClO_4$). Current–time transients were recorded after stepping a potential from +0.25 V to various final potentials ranging from 0.0 to −1.0 V.

Current–time transients are plotted on a log–log scale (Fig. 7A and B) and indicate a continuous decrease in current with time. The general trend is that the logs of measured currents are linearly dependent on the log of time throughout the measurement time (50 s). For the current–time data in the first second, the coefficient of determination

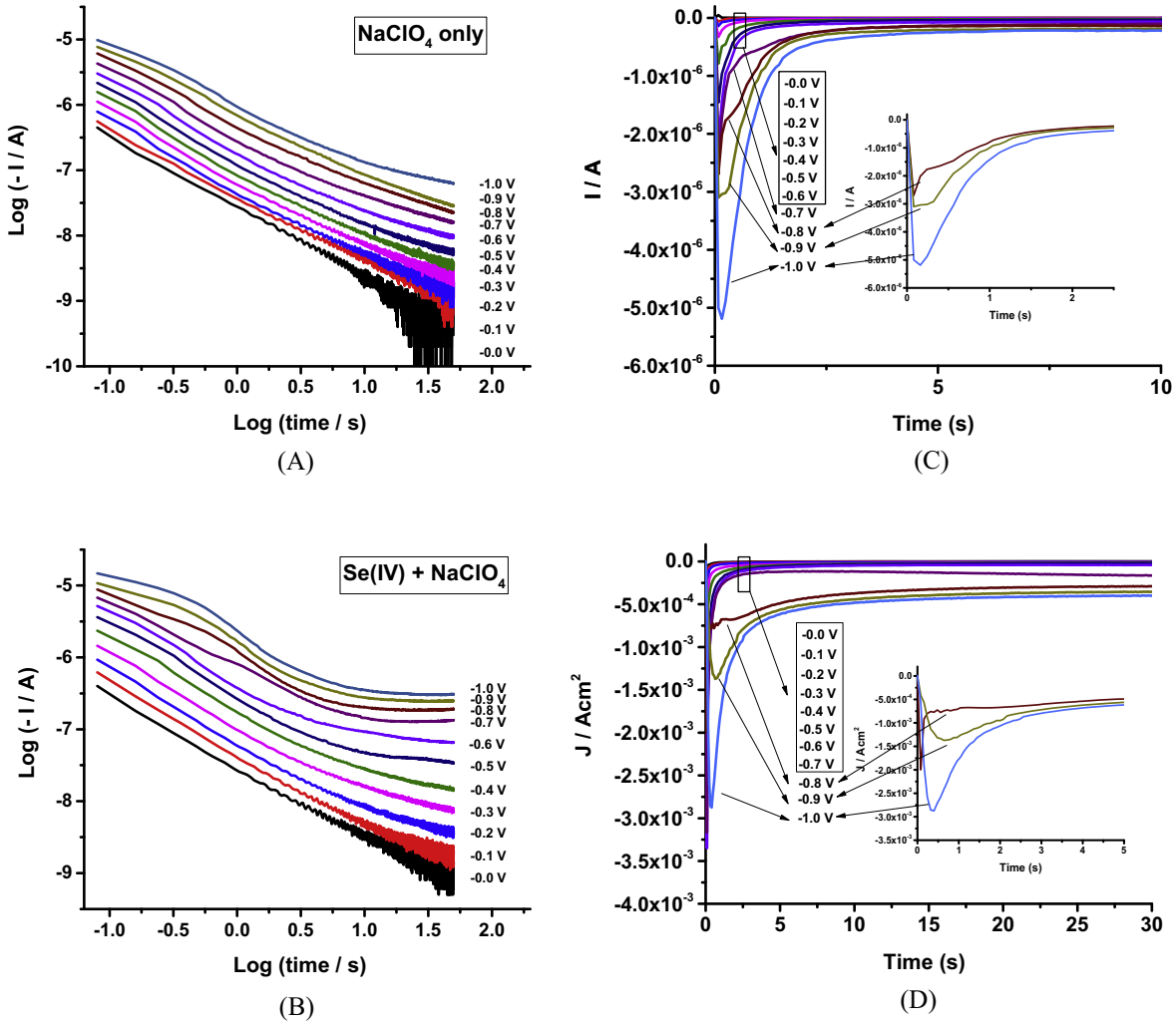

Fig. 7. Current–time transients recorded with the magnetite PME in (A) 0.1 M $NaClO_4$ and (B) 10 mM Na_2SeO_3 + 0.1 M $NaClO_4$, after stepping the potential from +0.25 V (30 s equilibrium) to various final potentials (50 s) as denoted in the graphs. (C) The blank curves (*i.e.*, (A)) were subtracted from the total current curves (*i.e.*, (B)) for the PME electrode and (D) for the bulk magnetite electrode (the blank and total current curves are not shown). In (C) and (D), the inlets show peak- or shoulder-shaped curves in the first few seconds.

Table 2
Chronoamperometry (during the first second of measurement) data linear-fitted in a log–log scale using the least square method.

Potential	0.1 M ClO_4			10 mM Se(IV) + 0.1 M ClO_4		
	m	*k*	R^2	*m*	*k*	R^2
0.0	−1.08	−7.57	0.998	−1.06	−7.58	1.000
−0.1	−1.07	−7.44	0.999	−1.08	−7.39	1.000
−0.2	−1.17	−7.38	0.999	−1.10	−7.23	1.000
−0.3	−1.18	−7.23	0.999	−1.08	−7.01	0.999
−0.4	−1.19	−7.09	0.998	−1.07	−6.76	0.997
−0.5	−1.17	−6.93	0.999	−1.08	−6.56	0.994
−0.6	−1.16	−6.76	0.997	−1.09	−6.41	0.993
−0.7	−1.13	−6.56	0.996	−0.87	−6.11	0.997
−0.8	−1.07	−6.34	0.996	−0.76	−5.87	0.988
−0.9	−0.99	−6.14	0.993	−0.76	−5.71	0.960
−1.0	−0.96	−5.99	0.988	−0.76	−5.55	0.944
Average	−1.11					
STDEV	0.08					

(R^2) was calculated using the least-squares method and exhibits good linearity ($R^2 > 0.90$) for all potentials tested (Table 2). Such linearity can be formulated as presented in Eq. (3).

$$\log(-I/A) = m\ \log(t/s) + k, \text{ and thus } I(t) = -(10^k)t^m \quad (3)$$

where m and k are the slope and intercept, respectively, measured in the log–log plots. The k value is proportional to current measured on the magnetite electrode, and the time dependence of the currents can be determined from the m value. The k value is greater in the selenium solution than in the blank solution for potentials between −0.1 and −1.0 V. The difference in the k value between the two solutions increases at more negative potentials. This implies that the contribution of selenium to the total electrical signal is enhanced as the potential decreases. There is no monotonic trend (*i.e.*, increase or decrease) in the m value for the blank solution as the potential varies. The m value averages to -1.1 ± 0.1 over a potential range from 0 to −1.0 V and thus the current–time transient, $I(t)$ is approximately proportional to $1/t$. At potentials $\geqslant -0.6$ V, the selenium solution shows comparable values of m to those of the blank solution whereas there are appreciable differences in the m value between the solutions at more negative potentials. Such differences can account for chemical processes involving the electroactive species on the electrode surface which can be observed within the initial 1 s.

Although the information from chronoamperometry is limited because of the pseudo-capacitance of the magnetite electrode, it is possible to distinguish the currents generated by magnetite from the total currents (Vielstich and Xia, 1995; Öznülüer and Demir, 2002). The current–time curves of the blank solution (*i.e.*, $NaClO_4$ only) were subtracted from those of the selenium solution (Se(IV) + $NaClO_4$) for each potential and are shown in Fig. 7C. The resulting curves show increments in the measured current as a potential becomes more negative. At potentials $\geqslant -0.6$ V, the cathodic currents rapidly decay within the first few seconds, but a significant change in the curve pattern is observed at potential $\leqslant -0.7$ V. Specifically, the peak or shoulder-shaped pattern is developed within the first second. The dependence of curve shape on the potential is also consistent with the interpretation on the m value described above. The time at which the center of the peak or shoulder shape appears (t_{max}) is measured within 0.15–0.7 s and becomes shorter with decreasing potential. Such patterns and time ranges of the current–time transients at the initial stage match well with a nucleation and growth process of selenium and other metals, which is recorded on the current–time curve in the first few hundred milliseconds to few seconds (Hölzle et al., 1994; Lai et al., 2010; Bougouma et al., 2013). The increase in peak current (I_{max}) and the decrease in peak time (t_{max}) indicate that the kinetics of Se deposition becomes faster as overpotential increases (Bougouma et al., 2013).

Experiments on metal electrodeposition are typically carried out using macroelectrodes (a few mm to a few cm in dimension). Therefore, chronoamperometry was also run using a bulk magnetite electrode in order to compare with the results from the magnetite PME. The experiments were performed with the selenium and blank solutions described above, and background curves were subtracted from total current curves. The resulting current–time curves are shown in Fig. 7D. At potentials $\leqslant -0.8$ V, the current density ($J = I/A$, a current per unit area) exhibits the peak- or shoulder-shaped pattern and the maximum values (J_{max}) are recorded between 0.35 and 2 s (t_{max}). The features on the observed curves are similar to those of the PME, although a longer time is needed for a peak or shoulder to appear on the curves. This delay indicates slower kinetics for Se deposition on the bulk electrode versus the PME. The shoulder-shaped pattern shown at potentials of −0.7 and −0.8 V for both the powder and bulk electrodes can be considered the current–time transient from the crystallization process superimposed on a falling transient at short times after double-layer charging (Hölzle et al., 1994). In the discussion section, the deposition of selenium on magnetite is examined theoretically and a possible nucleation mechanism is suggested.

3.2. XPS analysis for selenium redox chemistry on magnetite

XPS analysis was performed to examine redox chemistry of selenium on the magnetite electrode. The chemical reactions that represent the peaks observed on the CV curves can be related to specific selenium species produced at the peak potentials. Due to the geometry of the PME not being suitable for XPS analysis, all XPS samples were prepared from the bulk electrodes. The sample preparation was made at pH 6 using a solution containing 25 mM Na_2SeO_3 + 0.1 - M $NaClO_4$.

3.2.1. Cyclic voltammetry of bulk magnetite electrode prior to XPS analysis

Prior to the XPS analysis, the cyclic voltammetry was run using the bulk magnetite electrode and the electrochemical features were compared with the PME (Fig. 8). In the blank solution ($NaClO_4$ only), continuous increase in negative currents on the cathodic scan and small variation in positive currents on the anodic scan are similar to the background curves of the PME (Fig. 1A). In the presence of selenite (Se(IV) + $NaClO_4$), the cathodic currents begin to rise above the background signals at a potential below −0.1 V. A broad shoulder develops at potentials $\geqslant -0.6$ V where a peak C1 is pronounced on the cyclic PME voltammograms. The negative currents drastically increase at potentials < -0.6 V where the nucleation and growth process of selenium is promoted by large overpotentials. Upon anodic scanning, a single peak positioned at −0.25 V is produced which corresponds to peak A1 of the PME and the anodic current gradually decreases at more positive potentials. There is no observed CV peak or shoulder in the potential region where peak A2 is located in the PME results. Selenium redox transformation mediated by magnetite is greatly influenced by kinetic parameters and so the observed differences between the bulk electrode and PME may be due to the influence of the electrode properties on the redox kinetics. In particular, the bulk magnetite exhibits slower kinetics than the PME as evidenced by the

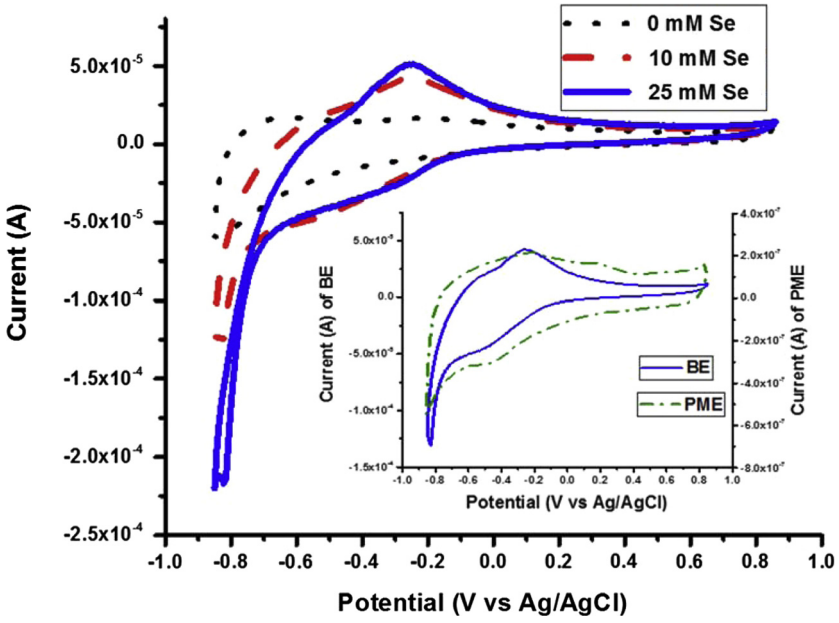

Fig. 8. Cyclic voltammograms for Se(IV) using the bulk magnetite electrode at pH 6.0 (scan rate = 50 mV/s; a scan range, −0.85 to +0.85 V). The scans were performed in solutions containing Se(IV) (10 and 25 mM) and 0.1 M $NaClO_4$. *Inlet*: Comparison of CV patterns measured (pH = 6.0 and [Se(IV)] = 10 mM) using the bulk electrode (BE) and the powder microelectrode (PME) of magnetite.

nucleation and growth of selenium (Section 3.1.4). The surface reactivity of solid materials as electrochemical catalysts is highly dependent on particle size. Smaller catalyst particles have higher density of reactive sites and thus typically exhibit greater rates of reaction with dissolved species (Nurmi et al., 2005; Peng et al., 2008; Yuan et al., 2015a, b). Nevertheless, the potential dependence of the cathodic and anodic currents (*i.e.*, the shape of CV curves) is comparable between the bulk electrode and PME (Figs. 2 and 8) which suggests similar redox transformation processes occur on the two electrode surfaces.

3.2.2. XPS results for selenium redox transformation

For the sample preparation, potential values were selected on the basis of the cyclic voltammograms at pH 6 (Figs. 2 and 8). Potentials of −0.5 and −0.2 V are where peaks C1 and A1 are approximately positioned, respectively, and −0.85 V corresponds to the switching potential in the voltammetry cycles performed in this study. A potential of +0.6 V was selected to examine possible redox reactions under very oxidizing conditions. Each potential was kept constant on a bulk electrode for 30 min. For the potential of −0.5 V, two additional samples were potential held and subsequently stepped to +0.2 and +0.6 V, respectively. These samples are intended to investigate any oxidation of selenium species produced at peak C1.

Survey scans on the magnetite electrodes are shown in Fig. 9. Observed peaks are labeled according to the corresponding orbitals of elements. The main peaks associated with Fe (Fe 2p and LMM) are clearly seen for all the magnetite electrodes. Two Auger peaks, $L_2M_{45}M_{45}$ and $L_3M_{45}M_{45}$ (denoted LMM and LMM′ in Fig. 9, respectively) and three XPS peaks, Se 3s, 3p, and 3d are associated with selenium on the electrode surface. The survey spectra show the presence of Se, Na, and Cl for all potentials tested, which are adsorbates from the background solution.

Core scans for the Se 3d peak are presented in Fig. 10A. The scan range also covers the binding energy corresponding to the Na 2p orbital (∼63 eV) as shown in the Se 3d spectra for all potentials tested. This orbital peak does not interfere with the Se 3d peak whose binding energies typically range from 62 to 53 eV (Wagner et al., 1979). Over such an energy range, two different peaks centered at about 55.5 and 58.5 eV are observed for all the potential-held electrodes. Sodium selenite was core-scanned as a reference material, which shows Se 3d peaks centered at 58.4 eV (Fig. 10A). Therefore, the XPS peak at ∼58.5 eV found from the electrode samples can be mainly attributed to Se(IV) despite the fact that there might be a minor contribution of Se(VI) if produced during the voltammetry scan on a positive potential range (*e.g.*, Alanyalioglu et al., 2004). Decrease in the oxidation state of an element leads to decrease in the electron binding energy of its orbitals. Therefore, the Se 3d peak centered at 55.5 eV, compared to the one at 58.5 eV, can indicate the presence of selenium with a lower valence state such as Se(0) or Se(−II). Bulk magnetite was analyzed as a reference sample and revealed a Fe 3p peak centered at about 55.5 eV. Interference of the Fe 3p peak with the Se3d peak also made it difficult to interpret the core-level spectra of selenium in previous studies (Hamdadou et al., 2002; Liu et al., 2007). To resolve this issue, the Se 3p peak was core scanned and compared with the Se 3d peak (Fig. 10B). Whereas of lower signal-to-noise ratio than the Se 3d spectra, the Se 3p spectra can be analyzed without the interference of the Fe orbitals. Peaks centered at 161.5 eV are found on the spectra of the electrodes held at −0.85 and −0.5 V and can be assigned to Se(0) and/

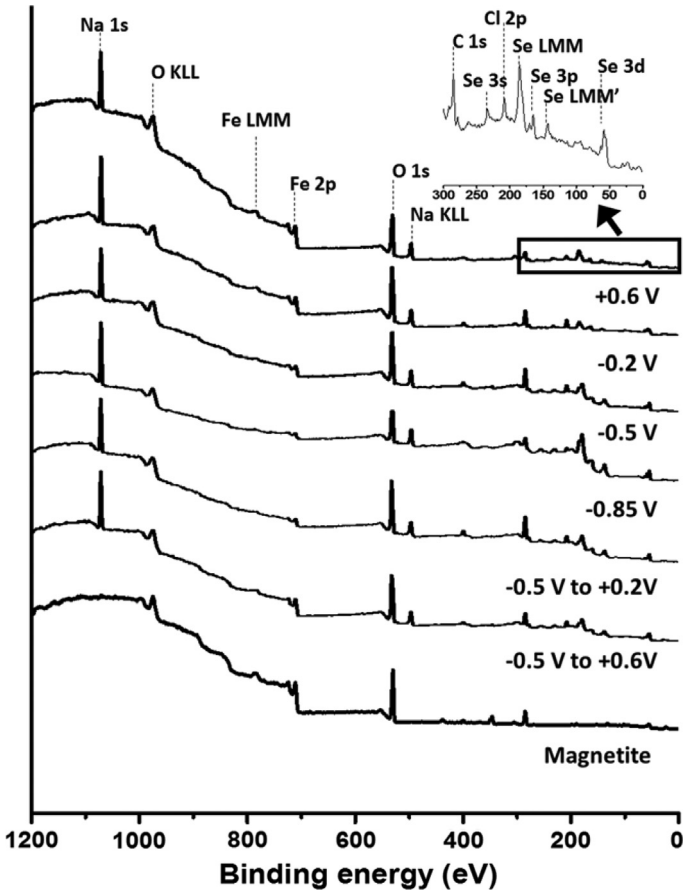

Fig. 9. XPS survey scans on the magnetite electrodes potential-held at various potentials. For the electrode at −0.5 V, two additional samples were stepped to positive potentials, +0.2 and +0.6 V, respectively, to re-oxidize the reduced products.

or Se(−II) (Mandale et al., 1984). In contrast, there are no observed peaks at 161.5 eV for the electrode of +0.6 and −0.2 V. The Se 3d spectra of these electrodes, therefore, should be identified as belonging to Fe 3p. It is also important to note that the peak at 55.5 eV appears as a doublet for the electrodes at −0.85 and −0.5 V and as a singlet for those at +0.6 and −0.2 V. The doublet feature is evidently different from the singlet feature observed on the Fe 3p of the magnetite reference.

For the Se 3d XPS peak, the binding energy between 56 and 55 eV is a commonly reported value for Se(0) (Wagner et al., 1979; Shenasa et al., 1986; Tang et al., 1996). The doublet appears at 55.0/55.8 eV, which is very close to the values for Se(0) reported from a previous study (Babu et al., 2007). In addition, a reddish deposit was observable by the naked eye on the magnetite electrode after it was held at a potential of −0.85 V for 30 min. This macroscopic observation indicates formation of elemental selenium on an electrode surface at a negative potential (Tang et al., 1996). The binding energy of Se(−II) 3d reported from many selenide compounds ranges from 55 to 53 eV depending on the nature of its coordinated atoms (Wagner et al., 1979; Shenasa et al., 1986; Hamdadou et al., 2002; Wu et al., 2007; Golovchak et al., 2013). As these ranges are close to the Se 3d peaks found in the present study, the minor presence of Se(−II) cannot be excluded. Se(0) is believed to dominate over Se(−II) given that at the high Se(IV) concentration of this study, Se(−II) produced at negative potentials can react with Se(IV) in solution to form elemental selenium in a comproportionation reaction (Wei et al., 1994) (Eq. (2)).

The spectroscopic results provide supportive evidence for the peak assignments on the cyclic voltammograms. There is no detected selenium species other than Se(IV) at the potential of −0.2 V. The reduction to elemental selenium is confirmed from the magnetite electrode held at −0.5 V. These results support the assignment of the broad C1 peak to the formation of Se(0). The predominance of elemental selenium on the electrode of −0.85 V is also in good agreement with the results of chronoamperometry that show how nucleation and growth mechanisms govern the selenium redox transformation under very reducing conditions (<−0.6 V). Elemental selenium is detected even if the electrode is stepped from −0.5 to +0.2 V or to +0.6 V (Fig. 10). Although the thermodynamic interpretation suggests that elemental selenium can be oxidized to Se(IV) at positive potentials, the interpretation for the selenium oxidation is limited from the XPS results because Se(IV) was detected in all the electrodes tested. The electrode held at +0.6 V shows no evidence for oxidation

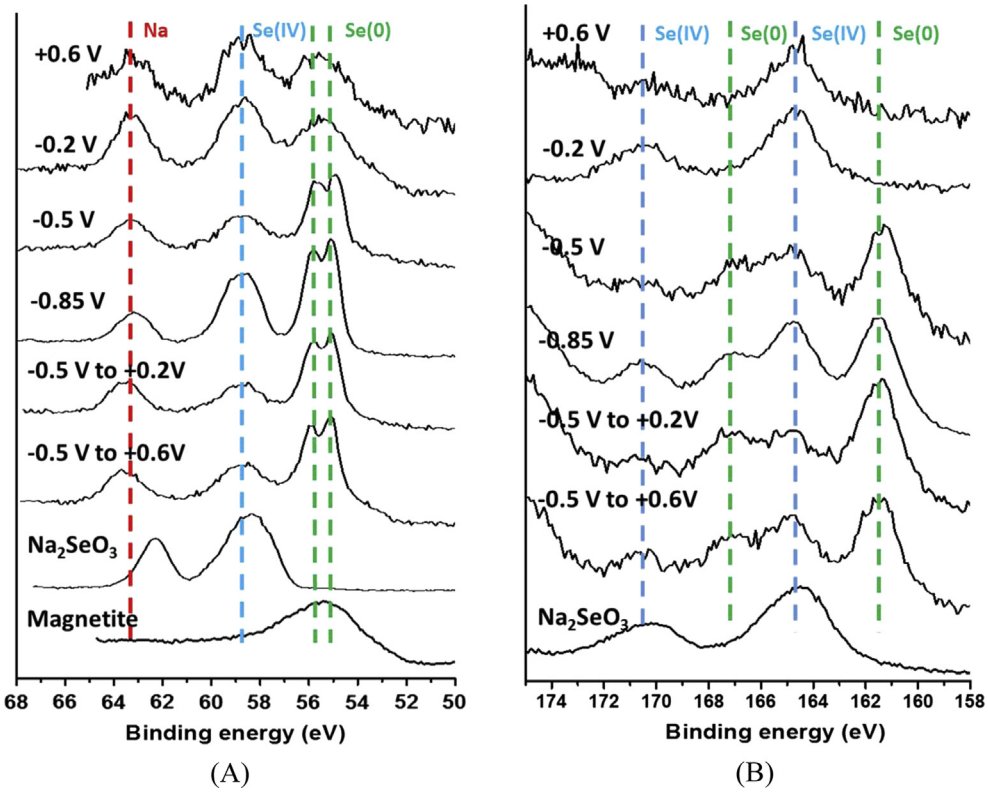

Fig. 10. XPS core scans for (A) Se 3d and (B) Se3p on the magnetite electrodes potential-held at various final potentials.

of Se(IV) to Se(VI). This may be due to the fact that Se(VI) formed at high potentials is immediately released into solution. If this was the case, only a minute amount of selenate could be retained on the electrode and would be undetectable by XPS. No clear indication is found for the transformation of selenite to selenate based on the electrochemical and spectroscopic approaches used in this study. Future research could be aimed at systematic investigation on the oxidation of Se(0) and Se(IV).

4. DISCUSSION

4.1. Possible effects of solution chemistry on Se redox transformation

CV peaks indicating selenium redox transformations on magnetite are evident at pH 4.0–8.0 but are of limited intensity at pH 9.5 (Fig. 2). Such pH dependence of the Se redox sensitivity is closely associated with the variation of Se solution chemistry. The speciation calculations demonstrate that Se(IV) is mainly present as biselenite ($HSeO_3^-$) at pH 3.0–8.0 whereas selenite (SeO_3^{2-}) is predominant at pH $\geqslant$9.0 (Fig. 6) It is thus inferred that biselenite is redox-active on magnetite in weak acids and bases (*i.e.* circumneutral pH values) whereas magnetite catalysis of selenite redox transformation is limited under high pH conditions (where SeO_4^{2-} is the dominant species). One hypothesis to explain this relationship between redox sensitivity and Se speciation is that the affinity of a given selenium species for the magnetite surface changes as a function of pH (Martinez et al., 2006; Rovira et al., 2008) and this may impact the surface concentration of Se available to participate in magnetite-mediated redox transformations. The point of zero charge of magnetite is near a pH of 7 (Tewari and Mclean, 1972), which implies that positively and negatively charged species can be retained on its surface at basic and acidic solutions, respectively. It follows that adsorption of Se(IV) on magnetite, as SeO_3^{2-} or $HSeO_3^-$ decreases with increasing pH as the magnetite surface becomes more negative (Martinez et al., 2006; Jordan et al., 2009; Missana et al., 2009). This may explain the absence of observable Se redox transformation at pH 9.5 in this study.

In comparison to thermodynamic data, the peak potentials fall into equilibrium reduction potential regions that correspond to the redox couples of interest (Fig. 5). However, the pH dependence of peak potentials is less pronounced than that predicted from equilibrium reduction potentials. For example, peak A2 was assigned to oxidation of Se(0) to Se(IV); therefore, from the ratio of the protons consumed *vs.* electrons accepted, a pe/pH slope of −5/4 (Eq. (4a)) is expected, resulting in a slope of −74 mV (5/4×59 mV, which is the Nernstian slope) per pH unit (Table 1). The observed slope of the potential change is ca. −21 mV per pH unit, or about three times lower. This reduction reaction can be written in two ways:

$$HSeO_3^- + 4e^- + 5H^+ \leftrightarrow Se(s) + 3H_2O \quad (4a)$$

$$HSeO_3^- + 2H_2O + 4e^- \leftrightarrow Se(s) + 5OH^- \quad (4b)$$

In the following, we discuss two explanations:

1. In the theoretical derivation, one underlying assumption is that the pH does *not* change significantly as a result of the reaction, but due to the small reaction volume (*i.e.*, the pore volume in the PME could be considered the reaction volume) the number of protons consumed per volume may be high.
2. Since the slope of Eq. (4a) is −5/4, and the numerator is the number of protons consumed, if there is also a source that releases protons as a result of the reaction, or consumes hydroxide ions (Eq. (4b)), the slope of the reduction potential *vs.* pH would be diminished.

Quantification of explanation 1: In order to estimate the amount of protons released or consumed, the number of electrons can be calculated from the CV curves and converted to the number of protons. The proton *concentration* is then obtained by either dividing by the pore volume of the mineral powder or the entire volume of the reacted solution. The consumption of protons during reduction may increase pH and lead to the difference in pH between the cavity and bulk solution. Although protons are exchanged between the pore and bulk solutions by mass transfer, the effect of proton consumption may be important under our experimental conditions where solution pH is weakly acidic to basic and the total selenium concentration exceeds the proton concentration.

The electronic charge transferred at peak C1 was calculated from a CV curve in Fig. 2 (pH 6.0 and 10 mM [Se]) as an example and the value is 1.07×10^{-6} C. This value was obtained by integrating the current peak over the voltage and dividing this value by the scan rate of, in this case, 50 mV/s. By dividing the charge value by the electron charge, one obtains 6.7×10^{12} electrons to be transferred. According to Eq. (4a), this value has to be multiplied by 5/4 to obtain the number of protons being consumed, which is 8.3×10^{12} protons or 1.4×10^{-11} mol of H^+. The *concentration* of protons consumed by the reduction can be evaluated considering the total volume of the microcavity ($\sim 1.2 \times 10^{-10}$ L; radius of the cavity ≈50 μm, depth ≈30 μm, porosity about 0.5). The calculated charge is equivalent to a proton concentration of 0.12 M in reference to the microcavity volume. This value is five orders of magnitude greater than the solution proton concentration (10^{-6} M) indicating that the cavity proton concentration is decreased by selenite reduction. An easier way to interpret this process is using Eq. (4b) which states that an equivalent amount of OH^- would be produced and would push the pH to high values. The minimum change in proton *concentration* can be estimated if one assumes that the reaction volume mixes with the entire volume of the vessel (50 mL). This would result in a proton concentration change of 1.4×10^{-11} mol/0.05 $L = 2.8 \times 10^{-10}$ mol/L, which is essentially no change in pH. Any local pH change induced by this reduction would be between these two extreme values due to the exchange of liquid between the microcavity pores and the bulk solution. This indicates that anyone performing redox reactions in a porous medium in contact with an aqueous solution may have a significant pH gradient between the medium and bulk solution; the same is true for a microporous soil with redox activity in contact with solution flowing through larger cracks. Due to the interdependence of pe and pH, there may also be a wide range of redox potentials for a specific redox transition in porous media where the water does not mix well.

Quantification of explanation 2: as Se(IV) is reduced to Se(0), the produced Se(0) is adsorbed or precipitated on the magnetite surface, thereby replacing protons from the mineral surface. The net loss in proton per reaction step in Eq. (4a) is thus less than 5. While it is possible to lessen the pe/pH slope, it would be difficult to imagine that one Se(0) sorbed releases one proton, but five protons are consumed (Eq. (4b)) contributes largely to the observed reduction in slope.

As known from macroscopic examples, *e.g.*, as in acid mine drainage, redox reactions can have a significant influence on pH and vice versa. Here, we demonstrate the potential for creating a pH gradient of several pH units at the interface between small redox-active micropores and larger, at least mL-sized volumes of water. This is not only the case in an experimental setup like the one at the interface of a powder microelectrode but also in redox-active environments (*e.g.*, soils) where microporous clay aggregates are in contact with flow-through macro cracks. Since the potential of a redox transition is typically pH-dependent, this means, in turn, that the pH gradient also leads to a peak broadening with more solution-like pH values right at the interface and higher/lower pH values further away for reduction/oxidation reactions while the magnitude of the gradient is dependent on pore size and diffusion times (Barth et al., 2009; Borch et al., 2009). It would be challenging to measure and quantify those pH gradients that take place at a micrometer scale in a total volume on the order of tens of microns across, which is even below the size and resolution of pH microelectrodes.

4.2. Mechanism of selenium nucleation on magnetite

As shown from the electrochemical and spectroscopic measurements, selenite can be reduced to elemental selenium at a negative potential (<−0.2 V). The XPS spectra denoting a predominance of elemental selenium on the electrode of −0.85 V is in good agreement with the results of chronoamperometry that the nucleation and growth mechanism governs the selenium redox transformation under those negative potentials. The next challenge is to determine, in a more mechanistic and quantitative way, how Se(0) precipitation starts and crystal growth progresses.

For theoretical considerations, the current–time curves in Fig. 7C and D were fitted to the nucleation and growth model proposed by Scharifker and Hills (1983) (Fig. 11). The model suggests two kinetic mechanisms, *i.e.*, instantaneous and progressive nucleation to address the nucleation properties such as the nuclear number density and the nucleation rate. Instantaneous nucleation describes the process by which the nuclei are formed at the onset of the electrochemical current, while progressive nucleation describes the process where the nuclei are continuously formed during the crystal growth (Bijani et al., 2011). These two nucle-

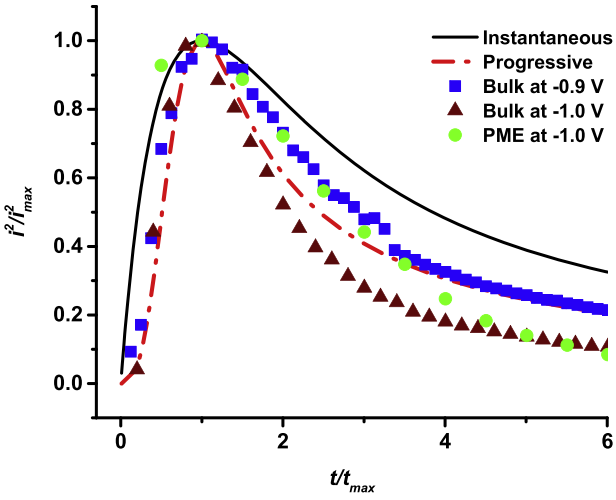

(A)

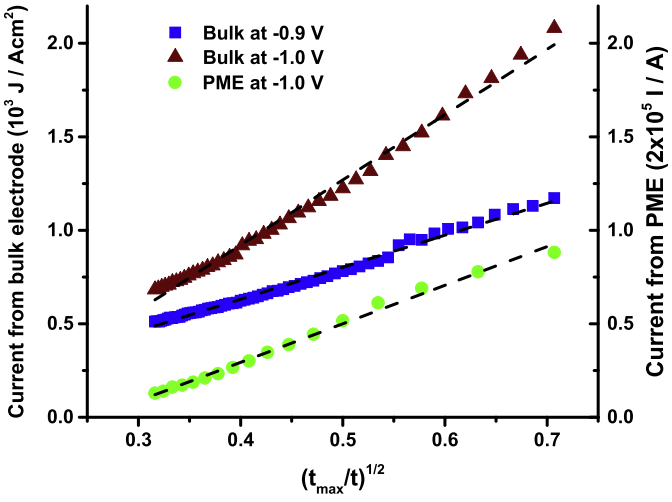

(B)

Fig. 11. (A) Comparison between the experimental transients (symbols) and the theoretical nucleation models (lines) in the dimensionless plot and (B) linear dependence between current and $t^{-1/2}$ for the falling portions of the transients over a time interval from $2t_{max}$ to $10t_{max}$.

ation processes are classically described by Eqs. (5a) and (5b).

$$\text{Instantaneous}: (I/I_{max})^2 = 1.95(t/t_{max})^{-1}\{1-\exp[-1.26(t/t_{max})]\}^2 \quad (5a)$$

$$\text{Progressive}: (I/I_{max})^2 = 1.23(t/t_{max})^{-1}\{1-\exp[-2.34(t/t_{max})^2]\}^2 \quad (5b)$$

All experimental transients in Fig. 11 (examples chosen are −1.0 V for PME and −1.0 and −0.9 V for the bulk electrode) show a peak in redox current at a certain time of the chronoamperometry experiment (t_{max}). The current and time values of the data were normalized to the current and time at each peak (I_{max} and t_{max}), respectively, and were compared with the multiple nucleation model (Fig. 11). The experimental curves fall closer to the theoretical model for the progressive nucleation (average residual $(I/I_{max})^2$ of 0.1) than to that for the instantaneous nucleation (average residual $(I/I_{max})^2$ of 0.2). On the rising portion of the curves ($t < t_{max}$), the slower increase in current for progress nucleation (compared to the instantaneous one) implies greater increment in the number of nuclei with time and slower nucleation than instantaneous nucleation (Scharifker and Hills, 1983).

There are, however, similarities and differences between the experimental data and theoretical progressive nucleation. The small positive deviation from the progressive model is observed on the rising portion of the fitting curves. This may be explained by contributions of other processes such as double layer charging and possibly adsorption–desorption processes (Scharifker and Hills, 1983; Hölzle et al.,

1994). Based on the assumptions of the model, a diffusion-controlled behavior is expected for long times and was evaluated on our data using the Cottrell relation (Eq. (6)).

$$I = \frac{zAFD^{1/2}c}{\pi^{1/2}t^{1/2}} \quad (6)$$

where I is the current, A the area of the electrode, z the number of electrons transferred on the reduction, F the Faraday constant, D the diffusion coefficient, c the bulk concentration, and t the time. The relation implies that the current is proportional to $t^{-1/2}$. In this application, caution should be taken since a planar electrode and unstirred solution are presumed for the strict application of the Cottrell relation. The bulk electrode used in this study is planar (Section 2.1) while the powder microelectrode obeys the Cottrell relation if the time of experiment is short (Yang et al., 1999; Zuleta et al., 2003). Thus the Cottrell relation was applied to the two types of electrode for a limited period of time (from 2 t_{max} to 10 t_{max}). For better illustration, I values were multiplied by large numbers and t^{-1} by t_{max}, respectively (Fig. 11B). The resulting current–time transients show excellent linearity ($R^2 > 0.99$), indicating nucleation as a diffusion-controlled process over the time range of interest. For the bulk electrodes, the diffusion coefficient was calculated from the Cottrell equation with the measured cross-sectional area (A) and the number of electrons transferred during the nucleation ($z = 4$ for selenite reduction to Se(0)). The values for the diffusion coefficient are 4.1×10^{-7} cm^2s^{-1} for -0.9 V and 10×10^{-7} $cm^2\,s^{-1}$ for -1.0 V. Alternatively, the diffusion coefficient can be derived from the nucleation model and the expression for progressive nucleation is presented in Eq. (7).

$$J_{max}^2 t_{max} = 0.2598 \cdot (zFc)^2 D \quad (7)$$

The calculated values are 3.1×10^{-7} $cm^2\,s^{-1}$ and 8.6×10^{-7} $cm^2\,s^{-1}$ for -0.9 and -1.0 V, respectively, comparable to the diffusion coefficients from the Cottrell equation. For both approaches, the diffusion coefficient observed at -1.0 V is about 2.5 times as great as that at -0.9 V which is at odd with the prediction from the multiple-nucleation model. Specifically, Scharifker and Hills (1983) suggested that for a given bulk concentration of electroactive species (10 mM Se(IV) in that case), the diffusion constant (D) should not vary with the potential. The inconsistency with the model is also seen on the falling portion of the curves where the experimental transients deviate negatively from the model for longer times ($t > 4t_{max}$). One possible source of the deviation from the theoretical model can be the morphology of the nuclei because the nuclei are considered hemispherical in the model (Grujicic and Pesic, 2002). The growth of nuclei under other mechanisms was postulated from a study regarding Rn deposition on a gold electrode (Schrebler et al., 2001). Another possibility is the beginning of H_2Se evolution followed by the comproportionation reaction with Se(IV) or hydrogen evolution at very negative potentials (Schrebler et al., 2001; Steponavicius et al., 2011). In summary, the interpretation of Se nucleation with the ideal model is limited as the reaction proceeds for long times. Nevertheless, in this study, the early stage of the peak-shaped current–time transients can be explained with the progressive 3-D nucleation model.

There have been a few studies adopting the multiple-nucleation model to investigate the mechanisms on electrodeposition of selenium on various electrodes. Lai et al. (2010) examined selenium deposition on a tin oxide electrode over a potential range of -0.4 to -0.6 V where a good agreement with progressive nucleation is observed. Glassy carbon was tested as a substrate for selenium deposition and revealed consistency with the progressive nucleation mechanism (Steponavicius et al., 2011). Although these reports employed aqueous solvents at room temperature, the instantaneous nucleation may occur under other physicochemical settings. Bougouma et al. (2013) suggested that the Se deposition kinetics is largely dependent on temperature and that slower progressive nucleation is favored at ambient temperature, whereas instantaneous nucleation is likely at higher temperatures (*e.g.*, 110 °C in a non-aqueous solvent). Our data support the progressive nucleation as a dominant mechanism for selenium deposition under ambient temperature and highly reducing conditions.

4.3. Catalysis of magnetite in geochemical systems

In natural environments, the abiotic reduction of trace elements can be mediated by a mineral surface when the reduction is coupled with the oxidation of other species on the surface. Dissolved Fe(II), for instance, does not seem to act as a reductant, but Fe(II) involved in a heterogeneous system enables trace elements to be reduced (Charlet et al., 2007; Taylor et al., 2015). Charlet et al. (2007) demonstrated the role of Fe(II) adsorbed by clay minerals in reducing selenium and helping form nanoparticulate Se(0). Selenium reduction can also be facilitated by oxidation of iron mineral surfaces and gives rise to products such as elemental selenium and iron selenides (Myneni et al., 1997; Scheinost and Charlet, 2008).

Our results from electrochemical experiments show that magnetite can act as a good substrate for selenite reduction and elemental selenium is formed as a primary product. While, in the electrochemical part of this study, electron transfer is triggered by applying an electrical potential, the mineral surface oxidation or the adsorption of reductants from solution to the surface can play an equivalent role in natural systems (Renock et al., 2013; Yuan et al., 2015b). Under a range of environmental conditions (pH 1–7 and 2–65 °C), the oxidation of magnetite can be promoted in the presence of protons (H^+) or redox-active metal species (M^{z+}) dissolved in water and cause the formation of maghemite (γ-Fe_2O_3) (Eqs. (8a) and (8b)) (White et al., 1994; White and Peterson, 1996).

$$[Fe^{2+}Fe_2^{3+}]O_4 + 2H^+ \leftrightarrow \gamma Fe_2O_3 + Fe^{2+} + H_2O \quad (8a)$$

$$3[Fe^{2+}Fe_2^{3+}]O_4 + \left(\frac{2}{n}\right)M^{z+} \leftrightarrow 4\gamma Fe_2O_3 + Fe^{2+} + \left(\frac{2}{n}\right)M^{(z-n)+} \quad (8b)$$

As a result, the metal species can be reduced by participating in the surface oxidation process or subsequent heterogeneous reactions involving ferrous iron (Fe^{2+}) released from the process. The formation of maghemite can passivate the magnetite surface, resulting in two important effects: (1) magnetite, which is thermodynamically unstable in most soil environments, can persist over geological time scales and (2) the redox-catalytic ability of magnetite is limited by passivation of the oxidized surface (Peterson et al., 1997). It is also likely that the redox-catalysis rate of magnetite becomes slower as Se(0) is deposited on the mineral surface due to a similar passivation effect. Peterson et al. (1997) studied reduction of Cr(VI) in the presence of magnetite and calculated the thickness of the maghemite layer (T_{mh}, in nm) formed as a result of electron transfer from Fe^{2+} in magnetite to an oxidized species in solution and the formula can be written for the reduction of Se(IV) to Se(0) as Eq. (9a).

$$T_{mh} = 4[Se^0]N_a/(d_{Fe(2+)} \cdot A_s \cdot 10^{18}) \quad (9a)$$

$$\Gamma_{Se} = [Se^0]/A_s \quad (9b)$$

where $[Se^0]$ is the number of moles of Se^0 atoms reduced from Se(IV) on the magnetite surface, multiplied by 4 to account for 4 Fe^{2+} atoms oxidized for every Se(IV) reduced, N_a, Avogadro's number, $d_{Fe(2+)}$, the density of Fe^{2+} atoms in the magnetite structure (atoms nm^{-3}), and A_S, the magnetite surface area ($m^2\ g^{-1}$) multiplied by 10^{18} to convert m^2 to nm^2. $[Se^0]$ is calculated from a CV curve in Fig. 2 (pH 6.0 and 10 mM [Se]) using the same conditions for quantification 1 in Section 4.1 resulting in an approximated thickness of maghemite is 5.4 Å, which is on the order of magnitude of the one estimated in a previous study on Cr(VI) reduction catalyzed by magnetite (1–2.4 nm) (Peterson et al., 1997). The surface coverage of Se(0) (Γ_{Se}) is evaluated, according to Eq. (9b), for the same CV curve (pH 6.0 and 10 mM [Se]) and is 0.30 nmol cm^{-2}. This corresponds to 15% coverage (0.15 ML) of the theoretical surface coverage for a metal monolayer (ML) on a substrate (2 nmol cm^{-2}) (Gerischer and Tobias, 1978; Beni et al., 2004). These estimated values imply that, in aqueous systems, the oxidation of unreacted magnetite particles may catalyze reaction pathways of selenite reduction as observed in this study, coupled with the formation of an oxidized layer that is a few to tens of Å thick. The catalytic ability of magnetite would likely degrade over time as the mineral surface is passivated by reaction products (Peterson et al., 1997; Ruiz et al., 2000).

In the experiments presented here, a high concentration of Se(IV) (1–25 mM) was required to differentiate the electrical signal of selenium species from the large background current of magnetite. This high selenium content may be one reason for the dominance of elemental selenium as a reduction product. Ferrous iron can be generated from magnetite dissolution at very reducing conditions (Section 3.1.1) and may play a role in the preservation of selenium species Se(−I) or Se(−II) as solid phases. Ferroselite ($FeSe_2$) is a stable compound of iron and selenium and is found in metal deposits bearing iron sulfides with high selenium content (Howard, 1977). The coexistence of elemental selenium and iron selenides with structures similar to FeSe and Fe_7Se_8 were found when a batch reaction of selenite with magnetite nanoparticles was maintained longer than the timescale of this study (Scheinost and Charlet, 2008). Therefore, in reducing environments where reactive iron is abundant, negative oxidation states of selenium are expected to be common.

5. CONCLUSIONS

In this study, electrochemical techniques are used to evaluate possible redox processes catalyzed by magnetite over a range of experimental conditions (Eh 1.09 to −0.77 V or 0.85 to −1.0 V *vs.* Ag/AgCl; pH 4.0–9.5). Biselenite ($HSeO_3^-$) can act as a redox-sensitive species under those conditions. Reaction pathways catalyzed by magnetite involving reduction of selenite and oxidation of reduced products are identified from the electrochemical and spectroscopic measurements. A soluble selenium oxyanion, Se(IV), is transformed into Se(0) or Se(−II) on the magnetite surface as it encounters reducing conditions (Eh = −0.27 V). Se(0) is directly deposited on the mineral substrate whereas adsorbed Se(−II) can undergo a subsequent comproportionation reaction with Se(IV) in solution to form Se(0). These reduced species can be remobilized to Se(IV) if exposed to oxidizing conditions (Eh = +0.44 V). Formation of soluble Se(VI) from oxidation of the lower valence forms may be mediated by magnetite, but since this study focuses on solid-state processes, no spectroscopic evidence is available for further oxidation in solution. The pH-dependence of the redox transformation of selenium may become significant in the microporous structure of soils or sediments due to a pH gradient formed at the particle-solution interface and the gradient between different pores with little tortuosity when pH changes are induced by redox processes. This is particularly true when compared with the redox transformation in the solution phase where a more homogeneous distribution of Eh and pH values is found. The retention of selenium on the mineral substrate by abiotic reduction is energetically and kinetically facilitated at low redox potentials. From chronoamperometry measurements, the kinetics of the retention mechanism is characterized mainly by the simultaneous nucleation and growth of elemental selenium (*i.e.*, progressive nucleation) under ambient temperature and highly reducing conditions (Eh < −0.47 V). The XPS analysis on the potential-stepped magnetite electrodes implies that once deposited on magnetite, remobilization of elemental selenium to soluble species would be partially irreversible and kinetically retarded. Therefore, magnetite can act not only as a catalyst for redox reactions of selenium but also as a substrate to retain selenium in an immobilized form. These findings demonstrate that the effect of natural minerals on the thermodynamics and kinetics of electron transfer is an important factor in predicting selenium mobility and reactivity in sediments and natural waters.

ACKNOWLEDGEMENT

The authors are grateful for the support from the U.S. National Science Foundation, Division of Earth Sciences, Grant No. EAR-1223976. Y.K. acknowledges support from Samsung Scholarship.

REFERENCES

Alanyalioglu M., Demir U. and Shannon C. (2004) Electrochemical formation of Se atomic layers on Au (1 1 1) surfaces: the role of adsorbed selenate and selenite. *J. Electroanal. Chem.* **561**, 21–27.

Babu P. K., Lewera A., Chung J. H., Hunger R., Jaegermann W., Alonso-Vante N., Wieckowski A. and Oldfield E. (2007) Selenium becomes metallic in Ru–Se fuel cell catalysts: an EC-NMR and XPS investigation. *J. Am. Chem. Soc.* **129**, 15140–15141.

Bard A. J. and Faulkner L. R. (1980) *Electrochemical Methods: Fundamentals and Applications*. Wiley, New York.

Barth J., Grathwohl P., Fowler H., Bellin A., Gerzabek M., Lair G., Barceló D., Petrovic M., Navarro A. and Négrel P. (2009) *Mobility, Turnover and Storage of Pollutants in Soils, Sediments and Waters: Achievements and Results of the EU Project AquaTerra – A Review*. Springer.

Beni V., Newton H. V., Arrigan D. W., Hill M., Lane W. A. and Mathewson A. (2004) Voltammetric behaviour at gold electrodes immersed in the BCR sequential extraction scheme media: application of underpotential deposition–stripping voltammetry to determination of copper in soil extracts. *Anal. Chim. Acta* **502**, 195–206.

Bijani S., Schrebler R., Dalchiele E., Gabas M., Martinez L. and Ramos-Barrado J. (2011) Study of the nucleation and growth mechanisms in the electrodeposition of micro-and nanostructured Cu_2O thin films. *J. Phys. Chem.* **115**, 21373–21382.

Borch T., Kretzschmar R., Kappler A., Cappellen P. V., Ginder-Vogel M., Voegelin A. and Campbell K. (2009) Biogeochemical redox processes and their impact on contaminant dynamics. *Environ. Sci. Technol.* **44**, 15–23.

Bougouma M., Van Elewyck A., Steichen M., Buess-Herman C. and Doneux T. (2013) Selenium electrochemistry in choline chloride–urea deep eutectic electrolyte. *J. Solid State Electrochem.* **17**, 527–536.

Bouroushian M. (2010) *Electrochemistry of Metal Chalcogenides*. Springer Science & Business Media.

Bruggeman C., Maes A., Vancluysen J. and Vandemussele P. (2005) Selenite reduction in Boom clay: effect of FeS_2, clay minerals and dissolved organic matter. *Environ. Pollut.* **137**, 209–221.

Cachet-Vivier C., Vivier V., Cha C., Nedelec J.-Y. and Yu L. (2001) Electrochemistry of powder material studied by means of the cavity microelectrode (CME). *Electrochim. Acta* **47**, 181–189.

Cha C. S., Li C. M., Yang H. and Liu P. (1994) Powder microelectrodes. *J. Electroanal. Chem.* **368**, 47–54.

Charlet L., Scheinost A., Tournassat C., GrenEche J.-M., Géhin A., Fernández-Martı A., Coudert S., Tisserand D. and Brendle J. (2007) Electron transfer at the mineral/water interface: selenium reduction by ferrous iron sorbed on clay. *Geochim. Cosmochim. Acta* **71**, 5731–5749.

Grant F. (1985) Aeromagnetics, geology and ore environments, I. Magnetite in igneous, sedimentary and metamorphic rocks: an overview. *Geoexploration* **23**, 303–333.

Gerischer H. and Tobias C. W. (1978). , p. 446. Advances in Electrochemistry and Electrochemical Engineering.

Golovchak R., Calvez L., Petracovschi E., Bureau B., Savytskii D. and Jain H. (2013) Incorporation of Ga into the structure of Ge–Se glasses. *Mater. Chem. Phys.* **138**, 909–916.

Gorski C. A., Handler R. M., Beard B. L., Pasakarnis T., Johnson C. M. and Scherer M. M. (2012) Fe atom exchange between aqueous Fe^{2+} and magnetite. *Environ. Sci. Technol.* **46**, 12399–12407.

Grujicic D. and Pesic B. (2002) Electrodeposition of copper: the nucleation mechanisms. *Electrochim. Acta* **47**, 2901–2912.

Hamdadou N., Bernede J. and Khelil A. (2002) Preparation of iron selenide films by selenization technique. *J. Cryst. Growth* **241**, 313–319.

Hölzle M., Retter U. and Kolb D. (1994) The kinetics of structural changes in Cu adlayers on Au (1 1 1). *J. Electroanal. Chem.* **371**, 101–109.

Howard J. H. (1977) Geochemistry of selenium: formation of ferroselite and selenium behavior in the vicinity of oxidizing sulfide and uranium deposits. *Geochim. Cosmochim. Acta* **41**, 1665–1678.

Jordan N., Lomenech C., Marmier N., Giffaut E. and Ehrhardt J.-J. (2009) Sorption of selenium(IV) onto magnetite in the presence of silicic acid. *J. Colloid Interface Sci.* **329**, 17–23.

Lai Y., Liu F., Li J., Zhang Z. and Liu Y. (2010) Nucleation and growth of selenium electrodeposition onto tin oxide electrode. *J. Electroanal. Chem.* **639**, 187–192.

Liu X., Fattahi M., Montavon G. and Grambow B. Retention of Se (-II) onto pyrite under redox potential conditions. *Mobile Fission and Activation Products in Nuclear Waste Disposal*, 95.

Lovley D. R. (1993) Dissimilatory metal reduction. *Annu. Rev. Microbiol.* **47**, 263–290.

Mandale A., Badrinarayanan S., Date S. and Sinha A. (1984) Photoelectron-spectroscopic study of nickel, manganese and cobalt selenides. *J. Electron Spectrosc. Relat. Phenom.* **33**, 61–72.

Martinez M., Gimenez J., De Pablo J., Rovira M. and Duro L. (2006) Sorption of selenium (IV) and selenium (VI) onto magnetite. *Appl. Surf. Sci.* **252**, 3767–3773.

Missana T., Alonso U., Scheinost A. C., Granizo N. and García-Gutiérrez M. (2009) Selenite retention by nanocrystalline magnetite: role of adsorption, reduction and dissolution/co-precipitation processes. *Geochim. Cosmochim. Acta* **73**, 6205–6217.

Myneni S., Tokunaga T. K. and Brown G. (1997) Abiotic selenium redox transformations in the presence of Fe (II, III) oxides. *Science* **278**, 1106–1109.

Nurmi J. T., Tratnyek P. G., Sarathy V., Baer D. R., Amonette J. E., Pecher K., Wang C., Linehan J. C., Matson D. W. and Penn R. L. (2005) Characterization and properties of metallic iron nanoparticles: spectroscopy, electrochemistry, and kinetics. *Environ. Sci. Technol.* **39**, 1221–1230.

Nurmi J. T. and Tratnyek P. (2011) *Electrochemistry of Natural Organic Matter*. American Chemical Society.

Öznülüer T. and Demir Ü. (2002) Formation of Bi_2S_3 thin films on Au (1 1 1) by electrochemical atomic layer epitaxy: kinetics of structural changes in the initial monolayers. *J. Electroanal. Chem.* **529**, 34–42.

Peng F. F., Zhang Y. and Gu N. (2008) Size-dependent peroxidase-like catalytic activity of Fe_3O_4 nanoparticles. *Chin. Chem. Lett.* **19**, 730–733.

Peterson M. L., White A. F., Brown G. E. and Parks G. A. (1997a) Surface passivation of magnetite by reaction with aqueous Cr (VI): XAFS and TEM results. *Environ. Sci. Technol.* **31**, 1573–1576.

Peterson M. L., White A. F., Brown G. E. and Parks G. A. (1997b) Surface passivation of magnetite by reaction with aqueous Cr

(VI): XAFS and TEM results. *Environ. Sci. Technol.* **31**, 1573–1576.

Renock D., Mueller M., Yuan K., Ewing R. C. and Becker U. (2013) The energetics and kinetics of uranyl reduction on pyrite, hematite, and magnetite surfaces: a powder microelectrode study. *Geochim. Cosmochim. Acta* **118**, 56–71.

Ronov A. and Yaroshevsky A. (1969) Chemical composition of the earth's crust. *Earth's Crust Upper Mantle*, 37–57.

Rovira M., Giménez J., Martínez M., Martínez-Lladó X., de Pablo J., Marti V. and Duro L. (2008) Sorption of selenium (IV) and selenium (VI) onto natural iron oxides: goethite and hematite. *J. Hazard. Mater.* **150**, 279–284.

Ruiz N., Seal S. and Reinhart D. (2000) Surface chemical reactivity in selected zero-valent iron samples used in groundwater remediation. *J. Hazard. Mater.* **80**, 107–117.

Saji V. S. and Lee C.-W. (2013) Selenium electrochemistry. *RSC Adv.* **3**, 10058–10077.

Santos M. C. and Machado S. A. S. (2004) Microgravimetric, rotating ring-disc and voltammetric studies of the underpotential deposition of selenium on polycrystalline platinum electrodes. *J. Electroanal. Chem.* **567**, 203–210.

Scharifker B. and Hills G. (1983) Theoretical and experimental studies of multiple nucleation. *Electrochim. Acta* **28**, 879–889.

Scheinost A. C. and Charlet L. (2008) Selenite reduction by mackinawite, magnetite and siderite: XAS characterization of nanosized redox products. *Environ. Sci. Technol.* **42**, 1984–1989.

Schrebler R., Cury P., Orellana M., Gómez H., Córdova R. and Dalchiele E. (2001) Electrochemical and nanoelectrogravimetric studies of the nucleation and growth mechanisms of rhenium on polycrystalline gold electrode. *Electrochim. Acta* **46**, 4309–4318.

Shenasa M., Sainkar S. and Lichtman D. (1986) XPS study of some selected selenium compounds. *J. Electron Spectrosc. Relat. Phenom.* **40**, 329–337.

Steponavičius A., Šimkūnaitė D., Valsiūnas I. and Baltrūnas G. (2011) Initial stages of selenium electrodeposition onto glassy car bon electrode. *Chemija* **22**.

Stumm W. and Sulzberger B. (1992) The cycling of iron in natural environments: considerations based on laboratory studies of heterogeneous redox processes. *Geochim. Cosmochim. Acta* **56**, 3233–3257.

Tang H., Kitani A. and Shiotani M. (1996) Electrochemical formation of polyaniline in selenic acid. *J. Electrochem. Soc.* **143**, 3079–3082.

Taylor S., Marcano M., Rosso K. and Becker U. (2015) An experimental and ab initio study on the abiotic reduction of uranyl by ferrous iron. *Geochim. Cosmochim. Acta* **156**, 154–172.

Tewari P. and McLean A. (1972) Temperature dependence of point of zero charge of alumina and magnetite. *J. Colloid Interface Sci.* **40**, 267–272.

Vielstich W. and Xia X. (1995) Comments on "Electrochemistry of methanol at low index crystal planes of platinum: an integrated voltammetric and chronoamperometric study". *J. Phys. Chem.* **99**, 10421–10422.

Wagner C., Riggs W., Davis L., Moulder J. and Muilenberg G. (1979) *Handbook of XPS*. PerkinElmer, Waltham.

Wang S.-Y., Ho K.-C., Kuo S.-L. and Wu N.-L. (2006) Investigation on capacitance mechanisms of Fe_3O_4 electrochemical capacitors. *J. Electrochem. Soc.* **153**, A75–A80.

Wei C., Myung N. and Rajeshwar K. (1994) A combined voltammetry and electrochemical quartz crystal microgravimetry study of the reduction of aqueous Se(IV) at gold. *J. Electroanal. Chem.* **375**, 109–115.

White A. F. and Peterson M. L. (1996) Reduction of aqueous transition metal species on the surfaces of Fe(II)-containing oxides. *Geochim. Cosmochim. Acta* **60**, 3799–3814.

White A. F., Peterson M. L. and Hochella M. F. (1994) Electrochemistry and dissolution kinetics of magnetite and ilmenite. *Geochim. Cosmochim. Acta* **58**, 1859–1875.

Williams K. T. and Byers H. G. (1934) Occurence of selenium in pyrites. *Ind. Eng. Chem. Anal. Ed.* **6**, 296–297.

Wu N.-L., Wang S.-Y., Han C.-Y., Wu D.-S. and Shiue L.-R. (2003) Electrochemical capacitor of magnetite in aqueous electrolytes. *J. Power Sources* **113**, 173–178.

Wu X., Zhang Z., Zhang J., Ju Z., Shen D., Li B., Shan C. and Lu Y. (2007) Structural and electrical characterizations of single tetragonal FeSe on Si substrate. *J. Cryst. Growth* **300**, 483–485.

Yang W., Zhang G., Lu S., Xie J. and Liu Q. (1999) Electrochemical studies of $Li/Li_xMn_2O_4$ by using powder microelectrode. *Solid State Ionics* **121**, 85–89.

Yuan K., Ilton E. S., Antonio M. R., Li Z., Cook P. J. and Becker U. (2015a) Electrochemical and spectroscopic evidence on the one-electron reduction of U(VI) to U(V) on magnetite. *Environ. Sci. Technol.* **49**, 6206–6213.

Yuan K., Renock D., Ewing R. C. and Becker U. (2015b) Uranium reduction on magnetite: probing for pentavalent uranium using electrochemical methods. *Geochim. Cosmochim. Acta* **156**, 194–206.

Zuleta M., Bursell M., Björnbom P. and Lundblad A. (2003) Determination of the effective diffusion coefficient of nanoporous carbon by means of a single particle microelectrode technique. *J. Electroanal. Chem.* **549**, 101–108.

Associate editor: Alfonso Mucci